



1 **Evaluation of UTLS carbon monoxide simulations in GMI and**
2 **GEOS-Chem chemical transport models using Aura MLS observations**

3 Lei Huang¹, Jonathan H. Jiang¹, Lee Murray^{2,3}, Megan Damon⁴, Hui Su¹, Nathaniel Livesey¹

4 [1] {Jet Propulsion Laboratory, California Institute of Technology, Pasadena, CA }

5 [2] {NASA Goddard Institute for Space Studies, New York, NY }

6 [3] {Lamont-Doherty Earth Observatory, Columbia University, Palisades, NY }

7 [4] {NASA Goddard Space Flight Center, Greenbelt, MD }

8 Correspondence to: Lei Huang (Lei.Huang@jpl.nasa.gov)



9 **Abstract**

10 This study evaluates the distribution and variation of carbon monoxide (CO) in the
11 upper troposphere and lower stratosphere (UTLS) during 2004–2012 as simulated by two
12 chemical transport models, using the latest version of Aura Microwave Limb Sounder
13 (MLS) observations. The simulated spatial distributions, temporal variations and vertical
14 transport of CO in the UTLS region are compared with those observed by MLS. We also
15 investigate the impact of surface emissions and deep convection on CO concentrations in
16 the UTLS over different regions, using both model simulations and MLS observations.
17 Global Modeling Initiative (GMI) and GEOS-Chem simulations of UTLS CO both show
18 similar spatial distributions to observations. The global mean CO values simulated by
19 both models agree with MLS observations at 215hPa and 147 hPa, but are significantly
20 underestimated (> 40%) at 100 hPa. In addition, the models underestimate the peak CO
21 values by up to 70% at 100 hPa, 60% at 147 hPa, and 40% at 215hPa, with GEOS-Chem
22 generally simulating more CO at 100 hPa and less CO at 215hPa than GMI. The seasonal
23 distributions of CO simulated by both models are in better agreement with MLS in the
24 Southern Hemisphere (SH) than in the Northern Hemisphere (NH), with disagreements
25 between model and observations over some enhanced CO regions such as southern Africa.
26 The simulated vertical transport of CO shows better agreement with MLS in the tropics
27 and SH subtropics than NH subtropics. We also examine regional variations in the
28 relationships among surface CO emission, convection and UTLS CO concentrations. The
29 two models exhibit emission-convection-CO relationships similar to those observed by
30 MLS over the tropics and some regions with enhanced UTLS CO.



31 **1 Introduction**

32 Carbon monoxide (CO) plays multiple important roles in atmospheric chemistry and
33 radiation balance. In particular, it serves as the primary sink of the hydroxyl radical (OH)
34 (Logan et al., 1981) and is an important tropospheric ozone (O₃) precursor (Daniel and
35 Solomon, 1998). CO in the troposphere is mostly emitted from the surface as a byproduct
36 of incomplete combustion of carbon-based fuels, and it has primary sources from fossil
37 fuel and biomass burning as well as secondary sources from oxidation of methane and
38 other hydrocarbons (Jacob, 1999; Shindell et al., 2006). CO can be rapidly uplifted into
39 mid- and upper troposphere by convection, where it can be transported around the globe
40 (Jiang et al. 2007). With a typical lifetime of 1–2 months in the troposphere, CO has been
41 often used as a tracer for studying the transport of polluted air masses that originate in
42 regions of biomass burning or fossil fuel combustion (e.g., Edwards et al., 2006, Huang et
43 al., 2012).

44 Previous studies using both satellite observations and model simulations have shown
45 that CO has strong seasonal and interannual variations in the upper troposphere and lower
46 stratosphere (UTLS) (e.g., Schoeberl et al., 2006; Liu et al., 2007; Liu et al., 2010, 2013;
47 Huang et al., 2012, 2014). Temporal variations of CO in the UTLS are affected by many
48 factors, including surface emission and convection, each has different seasonal variations;
49 as well as photochemistry and transport, which can affect CO concentrations either
50 locally or across a long-distance. Schoeberl et al. (2006) studied vertical transport of CO
51 across UTLS by analyzing the “tape recorder” - the vertical and temporal variations of
52 CO observed by the Aura Microwave Limb Sounder (MLS) during August 2004 to
53 December 2005. Their study indicates that this CO “tape recorder” arises from combined



54 seasonal variations in both surface emissions and convective transport of CO into the
55 upper troposphere (UT). These can be simulated by the Global Modeling Initiative (GMI)
56 chemical transport model (CTM) forced by climatological emissions. Many other studies
57 also have shown that convolved seasonality in surface emissions and deep convective
58 activity combines to enhance CO fluxes from the surface to the UT resulting in seasonal
59 peaks of CO (e.g., Liu et al., 2007; Liu et al., 2010; Huang et al., 2012). Strong
60 interannual variation of CO in the UT has been found to be mainly associated with
61 intense drought-induced fires in Indonesia and South America during El Niño periods
62 (Liu et al., 2013; Livesey et al., 2013; Huang et al., 2014).

63 Although both surface emissions and convective transport could influence the
64 seasonal peaks of CO in the UTLS, the relative importance of each factor varies between
65 regions. Liu et al. (2007) suggested that high CO concentrations in the tropical UT during
66 boreal Spring are mainly caused by a number of intense convective events over Africa
67 and the Amazon that transport large amounts of fire-generated CO to the tropical
68 tropopause. Ricaud et al. (2007) found that the peak in CO at the tropopause over Africa
69 during boreal Spring largely results from convective and large-scale horizontal transport
70 pathways, regardless of source region. Further study by Huang et al. (2012) confirmed
71 that the locations and seasonality of the UT CO maxima in the tropics were strongly
72 correlated with the frequency of local convection over South America and Central Africa
73 during 2007. However, Schoeberl et al. (2006), using model simulations, argued that the
74 UT CO maximum mainly results from strong biomass burning in Indochina. Gonzi and
75 Palmer (2010) further found that the fractions of surface CO emissions transported to the
76 UT are lower over Africa and South America than over Indonesia during June to October



77 2006. Although the relationships among emissions, convection, dynamical transport and
78 UTLS CO abundance have been investigated by some observational studies (e.g., Jiang et
79 al., 2007; Huang et al., 2012; Livesey et al. 2013), it is still not clear whether models can
80 reproduce these relationships.

81 The ability of global CTMs to capture the processes driving CO temporal and spatial
82 variations needs to be evaluated with observations. However, most of the previous model
83 evaluation studies have been limited to comparison with in-situ surface data (e.g., Duncan
84 et al., 2007), in-situ aircraft field campaigns with limited spatial and temporal coverage
85 (e.g., Hudman et al., 2007), and ground- or satellite-based remotely sensed total column
86 or coarse resolution vertical profile data (e.g., Edwards et al., 2006; Gloudemans et al.,
87 2006; De Laat et al., 2007). There are also some model inversion studies on CO sources
88 (e.g., Heald et al., 2004; Kopacz et al., 2009), including a few studies using vertical CO
89 information from multiple satellite products (e.g., Kopacz et al., 2010). Shindell et al.
90 (2006) evaluated seasonal and spatial distributions of surface CO in 26 global
91 atmospheric chemistry models and found that these models generally underestimate
92 extratropical CO concentration in the Northern Hemisphere, although they typically
93 perform reasonably well elsewhere. Although total column comparisons provide an
94 advantage over in-situ surface comparisons for model validation in the free troposphere,
95 neither surface nor total column data were able to constrain the vertical structure of CO in
96 the models. Since 2004, the MLS instrument aboard the Aura satellite has been providing
97 CO vertical profile measurements in the UTLS, which have been widely used for CO
98 distribution and transport studies (e.g., Liu et al., 2010, 2013; Huang et al., 2012, 2014).
99 For example, Liu et al. (2010) evaluated CO transport in the GEOS-Chem CTM driven



100 by GEOS-4 and GEOS-5 assimilated meteorological fields and discussed the differences
101 with MLS observations. Huang et al. (2012, 2014) developed a method to automate the
102 identification of convective transport pathways of CO through a joint use of MLS and
103 A-Train satellite measurements and applied this method to study factors affecting the
104 seasonal and interannual variations of tropical UT CO.

105 This study aims to evaluate the CO concentration and its distribution and variation in
106 the UTLS during 2004–2012 simulated by two state-of-the-science CTMs using the latest
107 version (V4.2) of Aura MLS data. The two models we use are GMI and GEOS-Chem.
108 We will investigate whether the models can reproduce the relationships between surface
109 CO emissions, convection and UTLS CO concentration seen in proxy and direct
110 observations. Section 2 introduces the Aura MLS data and model simulations used.
111 Section 3 compares model-simulated climatological seasonal distributions, monthly
112 variations and tape recorder signal of CO in the UTLS with the MLS observations.
113 Section 4 analyzes and discusses the discrepancies in CO in the UTLS over selected
114 regions between the model simulations and MLS observations. Section 5 investigates the
115 convolved impacts of CO emissions and convection on UTLS CO concentrations in both
116 the satellite observation and model simulations. The main conclusions of this study are
117 summarized and discussed in Section 6.

118 **2 Data**

119 **2.1 Aura MLS Observations**

120 The MLS instrument aboard the Aura satellite was launched on 15 July 2004. Aura
121 has a sun-synchronous orbit at an altitude of 705 km, with equatorial crossing times at
122 1:45 a.m. and 1:45 p.m. local solar time and a 16-day repeat cycle. MLS makes



123 measurements of atmospheric composition, temperature, humidity and cloud ice in the
124 upper troposphere and stratosphere by measuring thermal microwave emissions from
125 broad spectral bands with a limb-viewing geometry (Waters et al., 2006). An advantage
126 of MLS is that its measurements can be obtained in the presence of ice clouds and
127 aerosols that prevent measurements by shorter wavelength infrared, visible and ultraviolet
128 techniques. MLS observes CO at 240 GHz, with a vertical resolution of ~5 km in the
129 UTLS and horizontal resolutions of ~6 km and 500–600 km across- and along-track,
130 respectively (Livesey et al., 2008). An earlier version of the MLS CO retrieval (V2.2)
131 was biased high by a factor of two at 215 hPa, although the morphology was generally
132 realistic (Livesey et al., 2008). In a later version (V3.3), the high positive bias at 215 hPa
133 was removed, but the impact of deep clouds on CO observations was considerably worse
134 (Livesey et al., 2011). The newest version (V4.2) of the MLS data (Livesey et al. 2015)
135 was released in July 2015, reduces the cloud impacts seen in V3.3 while avoiding the
136 biases associated with V2.2. Comparisons of UTLS CO between the new (V4.2) and
137 previous (V3.3) versions are discussed in Appendix A (Figs. A1 and A2). Only thick
138 clouds that are typically associated with deep-convective cores are observable by MLS
139 (Wu et al., 2008), thus MLS cloud ice water content (IWC) has been used as a proxy of
140 deep convection in previous studies (e.g., Jiang et al., 2011; Liu et al., 2013; Livesey et al.
141 2013). In this study, we use MLS V4.2 Level 2 CO and IWC data, screening the data
142 using recommended procedures (Livesey et al., 2015). The lowest usable retrieval level
143 for CO and IWC is 215 hPa, where the estimated single-measurement precisions are ~19
144 ppbv for CO and ~1.2 mg m⁻³ for IWC. The systematic uncertainty for CO at 215 hPa is



145 ± 30 ppbv and $\pm 30\%$, and generally $\pm 30\%$ at other UTLS pressure levels (Livesey et al.,
146 2015).

147 **2.2 GMI and GEOS-Chem Model Simulations**

148 **2.2.1 GMI Model**

149 The GMI is a global 3-D CTM that includes full chemistry for both the troposphere
150 and stratosphere. The GMI model is an assessment tool as part of the NASA Modeling,
151 Analysis, and Prediction (MAP) program. It is capable of multiyear simulations for
152 assessments of anthropogenic impacts on atmospheric composition and the role of
153 long-range transport of pollution (Rotman et al., 2001). The GMI model includes a
154 combined stratosphere-troposphere chemical mechanism with 124 species, 320 chemical
155 reactions, and 81 photolytic reactions. The chemical mechanism in the troposphere
156 includes a detailed description of tropospheric ozone, NO_x , and hydrocarbon
157 photochemistry (Bey et al., 2001a). Photolysis rates in the troposphere and stratosphere
158 are calculated by using the Fast-JX radiative transfer algorithm (Wild et al., 2000; Bian
159 and Prather, 2002), which is an efficient algorithm for calculating photolysis rates in the
160 presence of clouds and aerosols. Radiative and heterogeneous effects of aerosols on
161 photochemistry are included in this model. Biogenic emissions of isoprene and
162 monoterpenes are calculated online (Guenther et al., 2006). Surface methane is read from
163 climatological monthly files, and allowed to advect and react. Convective transport is
164 parameterized using the NCAR convection scheme (rain, cloud, and land-water-ice are
165 calculated online).

166 The time period of the GMI hindcast simulation is 1990–2012, with 1990–1994
167 considered as the hindcast spinup period. The meteorological fields are from the Global



168 Modeling and Assimilation Office (GMAO) Modern-Era Retrospective Analysis for
169 Research and Applications (MERRA) reanalysis (Rienecker et al., 2011). The MERRA
170 data have 72 vertical levels with a top at 0.01 hPa, and the horizontal resolution is $1/2^\circ$
171 latitude \times $2/3^\circ$ longitude, which has been degraded to 2° latitude \times 2.5° longitude for
172 input to the CTM. The biomass burning (BB) emissions used in the simulation are from
173 the Global Fire Emission Database version 3 (GFED3) (van der Werf et al., 2010). The
174 fossil fuel (FF) emissions are based on the Emission Database for Global Atmospheric
175 Research (EDGAR) v3.2 inventory for 2000, overwritten with regional inventories over
176 specific regions (Zhang et al. (2009) inventory for 2006 over Asia, EPA NEI 2005 over
177 USA, EMEP over Europe, BRAVO over Mexico, CAC over Canada). The year-to-year
178 variability in the FF emissions is calculated wherever the inventories have year-specific
179 information. Otherwise, scaling factors from GEOS-Chem model (van Donkelaar et al.,
180 2008) are used to make the FF emissions year-specific. However, at the time when the
181 GMI emissions were generated, the GEOS-Chem scaling factors ended in 2006, so for
182 2007–2012, the USA emissions were scaled based on EPA emission totals for each year
183 and the European emissions were scaled on a country-wide basis using national emissions
184 from EMEP, and the Asian emissions were scaled using the REAS inventory projections.
185 Biofuel emissions are from Yevich and Logan (2003) and EPA emission inventory.

186 **2.2.2 GEOS-Chem Model**

187 GEOS-Chem is a global 3-D CTM developed by the atmospheric chemistry group at
188 Harvard University and has been widely used around the world. It is driven by
189 assimilated meteorological observations from the NASA GMAO Goddard Earth
190 Observing System (GEOS) (Bey et al., 2001b). GEOS-Chem includes a fully-coupled



191 treatment of tropospheric O₃-NO_x-VOC chemistry and various types of aerosols (e.g.,
192 Park et al., 2003; Alexander et al., 2005), along with 155 species, 292 chemical reactions,
193 and 64 photolytic reactions. Chemistry is fully resolved in the troposphere, with a
194 linearized scheme applied in the stratosphere (Murray et al., 2013). Emissions in
195 GEOS-Chem are from the same several basic inventories as used by GMI, with annual
196 scaling factors applied to account for trends. As for GMI, the Fast-JX radiative transfer
197 algorithm is used in GEOS-Chem. Anthropogenic non-methane volatile organic
198 compounds (NMVOCs) are emitted from the REanalysis of the TROpospheric chemical
199 composition (RETRO) inventory (Schultz et al., 2007), except for propane and ethane,
200 which follow Xiao et al. (2008). Biogenic NMVOC emissions follow the Model of
201 Emissions and GAses from Nature (MEGAN), which vary monthly with observations of
202 leaf area indices from satellite and hourly with temperature, radiation, and precipitation
203 (Barkley et al., 2011). Surface methane concentrations are fixed each month to maps
204 interpolated from NOAA flask data, and allowed to advect and subsequently react.
205 Convective transport in GEOS-Chem is computed from the convective mass fluxes in the
206 meteorological archive, as described by Wu et al. (2007). In this study, we use the
207 simulations of GEOS-Chem version 9-02 (www.geos-chem.org) driven by MERRA
208 reanalysis, the same meteorological fields as the GMI simulations. Vertical resolution is
209 degraded from that of the MERRA inputs above 78.5 hPa but maintained at the MERRA
210 resolution below, resulting in 47 total layers. The simulation period is 2003–2012, with
211 January 2003 to April 2004 discarded as initialization. The model output data have a
212 horizontal resolution of 2° latitude × 2.5° longitude, and 47 vertical layers between the
213 surface and 0.01 hPa.



214 **2.2.3 Model/MLS Comparison Approach**

215 The 2004–2012 annual mean values and interannual standard deviation of CO budget
216 for GMI and GEOS-Chem are provided in Table 1. In general, CO emissions from fuel
217 and biomass burning are mostly the same, but the chemical production and loss rates of
218 CO in the troposphere are quite different between the two models. Both the GMI and
219 GEOS-Chem simulations were archived at monthly temporal resolution, with the same
220 horizontal resolution. GEOS-Chem provides model output on model levels whose
221 pressure varies in time, whereas GMI provides output at fixed pressure levels. To
222 compare the simulated and observed CO profiles, we first aggregate the daily Aura MLS
223 along-track CO profiles into 2° latitude \times 2.5° longitude grid boxes, and calculate
224 monthly averages of CO in each grid box. We then apply the MLS V4.20 CO averaging
225 kernels and a priori profiles to each model's simulated CO profiles to take into
226 consideration the vertical sensitivity of the MLS retrieval for a most consistent
227 comparison (Livesey et al., 2015). In this process, the modelled CO profiles are
228 interpolated to the 37 pressure levels of the MLS retrieval.

229 **3 Global Comparison between Models and Observation**

230 The climatological seasonal distributions of CO at 215 hPa as observed by MLS and
231 simulated by GMI and GEOS-Chem are shown in Figure 1. The seasonal average is
232 calculated as the 8-year average from December 2004 to November 2012. In general, the
233 locations of high CO are well simulated in GMI and GEOS-Chem versus the MLS
234 observations, except over Africa. MLS indicates that local maxima occur over central
235 Africa during DJF and southern Africa during SON (Huang et al., 2012), but the
236 simulated maxima were over West Africa during both of these two seasons. The



237 simulated CO values by both models are smaller than MLS observations, with an
238 underestimation of generally less than 20% for the global mean (80 °S–80 °N) CO
239 concentration (Table 2a). The largest underestimation occurs in MAM and JJA for both
240 models, with GMI (GEOS-Chem) showing 20% (22.1%) and 20.2% (19.5%) less mean
241 CO in MAM and JJA than MLS observations, respectively. Furthermore, peak simulated
242 CO concentrations are smaller than MLS observations by up to ~40% for all seasons. The
243 trans-Pacific transport of CO from East Asia in MAM and JJA to North America is much
244 weaker in the model simulations than shown in the observations. Continental outflow of
245 CO in the UT from the eastern US and West Africa to the Atlantic Ocean during JJA is
246 also poorly simulated by both models. The simulated CO distribution of GMI is quite
247 similar to that of GEOS-Chem (the correlation coefficient between the two maps for each
248 season is greater than 0.98), with the difference of mean CO less than 7% (Table 2a). The
249 mean and peak values of simulated CO in GEOS-Chem are generally less than those from
250 GMI at this level, especially over South America and Africa during DJF and SON (CO
251 peak in GEOS-Chem is ~20% less than that in GMI).

252 At 147 hPa, high CO concentrations are mainly found in the tropical and sub-tropical
253 latitudes, especially over South America and Africa (Fig. 2). During boreal Summer,
254 there is a broad maximum over South Asia driven by convection associated with the
255 Asian Summer monsoon (Fu et al., 2006). Compared with MLS observations, both
256 models underestimate CO concentrations poleward of 50 °. The underestimation is
257 generally less than 32% for the global mean CO concentration (Table 2b), with the largest
258 underestimation occurring in MAM for both models (32.4% for GMI, 31.5% for
259 GEOS-Chem). In addition, seasonal CO maxima are also underestimated by about 30–40%



260 in the tropics. The difference in mean CO concentration between the two model
261 simulations is generally less than 5%, with GEOS-Chem slightly larger than GMI during
262 all seasons except DJF (Table 2b). Maxima over South America and West Africa during
263 SON and DJF are greater in magnitude (~15%) in GMI than in GEOS-Chem, but the
264 latter shows a greater maximum over South Asia during JJA than the former. The largest
265 model-observation discrepancies occur at 100 hPa as shown in Figure 3. Both models
266 significantly underestimate the observed CO concentrations (note the different color
267 scales in Fig. 3) compared to MLS. The underestimation is larger than 40% for the global
268 mean CO concentration (Table 2c), with the largest underestimation occurring in MAM
269 for both models (47.8% for GMI, 44.8% for GEOS-Chem). Although the simulations
270 generally capture the local maxima in each season, the magnitudes are significantly
271 smaller than the observation. The underestimation of CO from GMI ranges from ~22% to
272 ~70% compared with MLS CO, while the underestimation from GEOS-Chem ranges
273 ~18–68%. Both model simulations show similar CO distributions to each other, but the
274 CO maxima in GMI are generally smaller than those in GEOS-Chem, with a maximum
275 difference of ~8.7% during JJA for the global mean CO (Table 2c).

276 The vertical distribution of zonal mean CO and its seasonal variations are shown in
277 Figure 4. In general, MLS CO shows a pipe-like maximum in the tropics from 200 hPa to
278 100 hPa, with a stronger vertical gradient above 100 hPa than below. However, the
279 simulations have more diffuse horizontal gradients in the UT and the vertical gradient of
280 CO is stronger below 100 hPa and weaker above 100 hPa than MLS. This may suggest
281 that upward transport of CO is underestimated in the models. Although the models
282 successfully reproduce a seasonal shift of local UT maxima from the tropics to the



283 northern subtropics from DJF to JJA, they fail to simulate the higher maxima in the
284 southern subtropics during SON. This is mainly due to the underestimation of CO
285 concentration in the UT over southern Africa and South America (Figs. 1 and 2). The two
286 models' simulations are quite similar, except some differences in magnitude below (i.e.,
287 at pressures larger than) 150 hPa during SON and DJF as previously shown in the CO
288 distribution map.

289 The temporal variability of the zonal mean monthly CO from 30°S to 30°N at 215
290 hPa for more than 8 years (August 2004 – December 2012) is shown in Figure 5. The
291 high CO concentrations observed in the northern tropics and subtropics are
292 underestimated in the models, especially from April to July when both models
293 underestimate by as much as 33%, which is significant compared to the MLS
294 measurement uncertainty. This is mainly due to the underestimated CO over South Asia
295 and East Asia as shown in Figure 1. As a consequence, the seasonal cycle of CO over this
296 latitudinal band is not well simulated. The temporal variation of CO in the southern
297 subtropics is well captured by GMI ($r=0.83$, $n=15$ latitudes \times 101 months) and
298 GEOS-Chem ($r=0.80$), except the magnitude is a little smaller than observation
299 (difference $< 10\%$). High CO values simulated by GMI during ENSO periods are
300 comparable with MLS CO, which is mainly related to stronger CO emissions generated
301 by drought-induced fires in Indonesia or South America compared to normal years (Liu et
302 al., 2013; Livesey et al., 2013; Huang et al., 2014). GMI shows higher CO values in the
303 tropics during DJF and SON than GEOS-Chem, especially in some El Niño-Southern
304 Oscillation (ENSO) years such as 2004-05, 2006-07 and 2010-11. The comparisons of
305 zonal mean CO between MLS and models at 147 hPa are similar to 215 hPa (figure not



306 shown). At 100 hPa (Fig. 6), the most distinctive feature is the semi-annual peaks with
307 similar magnitudes in boreal Spring and Fall as shown in MLS data. This semi-annual
308 variation of CO in the UT is mainly due to the temporal overlapping of surface biomass
309 burning from different continents and the inter-hemispheric shifts of deep convection
310 (Duncan et al., 2007; Liu et al., 2013). The two models significantly underestimate CO at
311 this level, and the peak during MAM is much weaker than the other peak during SON.
312 The semi-annual CO peaks during boreal Spring and Fall in GEOS-Chem are slightly
313 (~5%) larger than those in GMI.

314 Figure 7 shows the temporal evolution of monthly meridional mean tropical (15°S–
315 15°N) CO at 215 hPa. In general, GMI shows better agreement with MLS observation
316 than GEOS-Chem with respect to the locations and magnitudes of the high CO
317 concentration, since the magnitudes of CO peaks are weaker in GEOS-Chem than in GMI.
318 The correlation coefficients between observation and simulations are 0.78 and 0.81 for
319 GMI and GEOS-Chem, respectively (n=144 longitudes × 101 months). The seasonal
320 peaks over South America, Africa and Indonesia are well represented in the model
321 simulations, but their magnitudes are smaller than those observed, especially over Africa
322 and Indonesia. The maxima (~160–170 ppbv) over Indonesia during 2006-07 El Niño and
323 over South America during 2010-11 La Niña are well captured by the models. At 147 hPa,
324 the interannual variation of meridional mean CO is similar to that at 215 hPa, except that
325 the seasonal high CO encompasses a larger zonal area. At 100 hPa, the consistency
326 between the models and MLS is substantially worse, as indicated by the significant
327 underestimation (> 50%) of CO peaks and the locations of seasonal CO maxima (Fig. 8).
328 For example, MLS shows a local CO maximum (~90 ppbv) over Africa during



329 November-December 2007 that the simulations do not capture. Furthermore, MLS
330 detects clear semi-annual CO peaks over Africa, but the models only show one annual
331 peak. Overall, the average magnitude of CO in GEOS-Chem is ~5% larger than that in
332 GMI at this level.

333 Air masses can enter the stratosphere in the tropics, driven by adiabatic upwelling of
334 the Brewer-Dobson circulation (Brewer, 1949). During this slow upward transport,
335 seasonal and interannual variations in the mixing ratios of some trace gases are preserved,
336 as first observed in water vapor by Mote et al. (1995). This phenomenon is termed the
337 “tape recorder”. Schoeberl et al. (2006) identified the CO tape recorder for the first time
338 using MLS observations from August 2004 to December 2005. In this study, we evaluate
339 the model-simulated CO tape recorder by taking advantage of the multi-year MLS data
340 now available. Figure 9 shows the CO tape recorder (as a zonal mean between 15 °S and
341 15 °N). An 8-year mean (2005–2012) was subtracted from the monthly mean time series
342 at each level for MLS data and the two models’ simulations. In general, the observed and
343 simulated CO tape recorders show good agreement ($r=0.76$ for GMI, $r=0.81$ for
344 GEOS-Chem, $n=11$ levels \times 101 months). The observations and simulations show a
345 semi-annual cycle around 200 hPa and a strong annual cycle above 80 hPa. In the lower
346 stratosphere, both models show that the tape recorder signal fades out at approximately
347 the same altitude (~20 km) and the phase lines are quite similar to MLS observations. In
348 the upper troposphere, the two models simulate the interannual variation of CO during
349 the Northern and Southern Hemisphere fire seasons, which suggests that the surface CO
350 emissions account for most of the CO variation near the tropopause. The phase shift and
351 CO anomaly magnitude in GMI simulation are more consistent with MLS observation



352 than those in GEOS-Chem simulation. The models show that the location of the “tape
353 head” is near 200 hPa, which is in rough agreement with MLS. In addition, the strong
354 positive CO anomalies during three ENSO years (2004-05, 2006-07 and 2010-11) are
355 captured by both observation and models.

356 The CO tape recorder signal over northern subtropics (10–30 °N) is shown in Figure
357 10. In general, model simulated tape recorders are not consistent with observation, as
358 shown by a 2-3 month time lag between the same phases of CO peak anomaly. This
359 inconsistency may be caused by the underestimation of vertical transport in the models
360 (Schoeberl et al., 2006; Liu et al., 2010). Over this region, the ENSO signal is not as
361 strong in the MLS observations as that over the tropics, yet the two models still show
362 high positive CO anomalies during several ENSO periods. For the southern subtropics
363 (10–30 °S), MLS and models have much better agreement (Fig. 11). The seasonal peaks
364 and phase shift of CO anomalies are well collocated between observation and simulations.
365 GMI simulation is much closer to MLS observation than GEOS-Chem in magnitude.
366 However, the magnitude of positive anomaly in GMI simulation is still smaller than MLS
367 observation (except the 2006-07 El Niño year), which is mainly due to the
368 underestimation of surface CO emission over South America and southern Africa (Liu et
369 al., 2010, 2013).

370 **4 Regional Comparison between Models and Observation**

371 To further evaluate CO differences between observation and model simulations, we
372 examine six regions of high CO: South America (0–30 °S, 40–80 °W), Southern Africa (0–
373 30 °S, 10–40 °E), Northern Africa (0–30 °N, 15 °W–40 °E), East Asia (20–45 °N, 105–
374 145 °E), South Asia (10–30 °N, 70–105 °E), and Indonesia (10 °S–10 °N, 100–150 °E).



375 Figure 12 shows the climatological monthly mean of CO at 215 hPa from MLS and
376 the models over these regions. Both models underestimate the CO seen by the
377 observations throughout the year over three regions (southern Africa, East Asia, and
378 Indonesia). The largest underestimation by GMI (GEOS-Chem) is 19% (33%) over South
379 America, 30% (36%) over southern Africa, 22% (23%) over northern Africa, 37% (35%)
380 over East Asia, 31% (29%) over South Asia, and 22% (22%) over Indonesia. The
381 seasonal cycle of CO is similar between MLS and the models over South America
382 ($r=0.81$ for both models), southern Africa ($r=0.74$ for GMI, $r=0.75$ for GEOS-Chem),
383 East Asia ($r=0.76$ for GMI, $r=0.84$ for GEOS-Chem) and Indonesia ($r=0.92$ for GMI,
384 $r=0.95$ for GEOS-Chem) (Figs. 12a, 12b, 12d and 12f), although the magnitudes are
385 underestimated. Over these first two regions, MLS shows maxima in October; both
386 models greatly underestimate the peak value and fail to simulate the observed decreasing
387 trend from October to January. Over Indonesia, there is an average underestimation of
388 ~15% throughout the year. The underestimation of CO peaks over these regions may be
389 due to low biases in direct surface emission, the fraction of fire emissions released above
390 the boundary layer, biogenic NMVOC oxidation, and/or upward convective transport.
391 Over the remaining two regions, northern Africa and South Asia, simulated seasonal
392 variations are not consistent with MLS. For example, MLS shows CO peaks in August
393 for South Asia (Fig. 12e), but the peaks in both models lag MLS by one month. This is
394 probably due to insufficient representation of vertical transport in the CTMs or
395 underlying meteorological reanalysis. CO mixing ratios simulated by GMI are generally
396 larger than by GEOS-Chem, with differences typically less than 10%. However, the



397 model differences are larger from October to February over South America and Africa,
398 with a maximum of ~20% (Figs. 12a-c).

399 At 147 hPa, the differences in CO are similar to those at 215 hPa (figure not shown).
400 Compared with MLS, the largest underestimation by GMI (GEOS-Chem) is 26% (32%)
401 over South America, 35% (35%) over southern Africa, 28% (27%) over northern Africa,
402 33% (32%) over East Asia, 28% (25%) over South Asia, and 19% (18%) over Indonesia.
403 The differences in CO at 100 hPa between MLS and the models are shown in Figure 13.
404 The seasonal cycles are similar between MLS and models over South America, southern
405 Africa and Indonesia (Figs. 13a, 13b and 13f). The underestimation by the models
406 reaches maximum at this level. For example, the largest underestimation by GMI is 46%
407 over South America, 46% over southern Africa, 41% over northern Africa, 46% over
408 East Asia, 42% over South Asia, and 36% over Indonesia, compared with MLS. In
409 general, the temporal variations of GMI and GEOS-Chem are similar, but GMI is smaller
410 than GEOS-Chem over all regions, especially from May to October.

411 To evaluate the vertical distribution of CO in the UTLS, we present 8-year seasonal
412 mean CO profiles for each region (Fig. 14). Both models underestimate CO at all levels
413 observed by MLS below (i.e., with pressures greater than) 50 hPa. The magnitude of
414 underestimation depends on region, altitude and season. For instance, the difference
415 between MLS and GMI CO during JJA increases monotonically from 215 hPa to 100 hPa
416 over South America, whereas it first decreases (215 – 147 hPa) and then increases (147 –
417 100 hPa) over East Asia. This is also shown in earlier figures for the climatological
418 monthly mean of CO in the UTLS (Figs. 12 and 13). In general, the differences between
419 GMI and GEOS-Chem are largest at 215 hPa (up to 18%) and decrease with increasing



420 altitude. GMI mixing ratios are greater than GEOS-Chem at altitudes below (pressures
421 less than) 147 hPa over South America, Africa and Indonesia. However, it becomes
422 slightly less than GEOS-Chem for heights above (i.e., pressure smaller than) 100 hPa.
423 That the profile shapes are different, despite identical underlying meteorology, suggests
424 that the way in which each CTM parameterizes its convective transport (including
425 detrainment and entrainment) is affecting the resulting vertical distribution.

426 **5 Relation between Emission, Convection and UTLS CO**

427 In the sections above, we have evaluated the spatial distributions and temporal
428 variations of CO in the UTLS simulated by the two models, on both the global and
429 regional scale. Previous studies have shown that CO in the upper troposphere can be
430 affected by both surface emission and convection (e.g., Schoeberl et al., 2006; Liu et al.,
431 2007; Liu et al., 2010; Huang et al., 2012), thus it is important to evaluate the abilities of
432 models to simulate the relationships between surface emission, convection, and CO in the
433 UTLS. In this way, we can better understand the differences between observation and
434 simulation of CO in the UTLS.

435 The climatological monthly mean of surface CO emission from GMI (very similar to
436 GEOS-Chem), IWC and CO at three pressure levels from MLS are shown in Figure 15.
437 Each variable is normalized for comparison. MLS IWC is used here as a proxy of
438 convective intensity (“CONV” in Fig. 15). In general, seasonality in CO at 147 hPa is
439 similar to that at 215 hPa, but different from that at 100 hPa. The relationships between
440 UTLS CO and emission and convection vary with regions. For example, over South
441 America and southern Africa, the annual CO peak lags the emission peak by 1–2 months
442 at 215 and 147 hPa. Over East and South Asia, the annual CO cycle closely follows the



443 variation of convection at the two lower levels. Over northern Africa and Indonesia, it
444 seems that both emission and convection are important in determining CO in the UTLS.

445 Due to the complexity of the emission-convection-CO relationship, we apply a
446 bi-variate composite analysis (Jiang et al., 2007), and the results are shown in Figures 16
447 and 17 for CO at 215 hPa over the tropics (30°S–30°N) and different regions,
448 respectively. The monthly mean CO mixing ratios at 215 hPa in each grid box from MLS
449 observation and model simulations are binned according to the total (anthropogenic and
450 biomass burning) surface CO emissions (x-axis) and the convective (CONV) index
451 (y-axis). The CONV index is calculated as the IWC (from MLS observation) or
452 convective mass flux (from two models' simulations) value in each grid box divided by
453 the regional mean value at the same level. We have compared MLS IWC with convective
454 mass flux from the models and found that they have good linear correlation. The surface
455 CO emission data used for GMI simulation are reused for the MLS bi-variate composite
456 analysis. The color contour indicates the unity-based normalized CO value (i.e., 0 is the
457 minimum and 1 is the maximum) at each pressure level.

458 Over the tropics (Fig. 16), MLS shows that CO concentration at 215 hPa is high when
459 convection is strong. With the presence of deep convection ($\text{CONV} > 1$), CO generally
460 increases with increasing surface emission. When convection is relatively weak (CONV
461 < 0.1), CO is generally low and bears little connection with surface emission. CO
462 concentration reaches maximum when both convection and emission are strong. When
463 emission is very weak, the variation of CO may result from long-range transport
464 preceding convective lofting (Huang et al., 2012). For example, MLS shows a high CO
465 center when emission is relatively weak (between 0.02–0.1 g/m²/month) and convection



466 is strong ($\text{CONV} > 2$), which is also captured in the GMI simulation. In general, both
467 GMI and GEOS-Chem simulations show similar emission-convection-CO relationships
468 compared with MLS observation, except the slope of CO contours has some differences.
469 For instance, GMI seems to overestimate CO when convection is moderate ($0.05 <$
470 $\text{CONV} < 1$) or emission is strong ($> 1 \text{ g/m}^2/\text{month}$), while GEOS-Chem underestimates
471 CO when convection is strong ($\text{CONV} > 1$) with weak emission ($< 0.1 \text{ g/m}^2/\text{month}$). At
472 147 hPa, the emission-convection-CO relationships are similar to those shown at 215 hPa.
473 For MLS observations, CO increases with emission when convection is moderate or
474 strong ($\text{CONV} > 0.1$), but the high CO shown at 215 hPa when emission is weak with
475 strong convection is less pronounced at this level. The emission-convection-CO
476 relationships simulated by GMI and GEOS-Chem also show similarity to MLS
477 observation at 147 hPa, despite some differences in the slope of CO contours. At 100 hPa,
478 the emission-convection-CO relationships simulated by the two models are quite different
479 from MLS observation (figure not shown), probably due to the significantly
480 underestimated convection and CO in the models at this level, thus we do not discuss
481 them in detail here. For the regional discussion below, we will also only focus on 215 hPa
482 and 147 hPa.

483 Over the six different regions (Fig. 17), MLS shows that CO concentrations at 215
484 hPa are generally high when emission and convection are strong. However, there are also
485 distinct regional differences. Over South America, CO does not change much when
486 convection is relatively weak ($\text{CONV} < 1$), even though strong emission is present. CO
487 increases rapidly when emission is large ($> 1 \text{ g/m}^2/\text{month}$) with strong convection. This
488 suggests that local convection plays an important role in determining CO mixing ratio in



489 the UT over this region, which has been demonstrated by previous studies (e.g., Huang et
490 al., 2012). Over southern and northern Africa, two high CO centers occur when
491 convection is strong ($CONV > 1$), one is located in a weak emission regime ($0.02\text{--}0.1$
492 $\text{g/m}^2/\text{month}$), and the other is accompanied by strong emission ($> 0.5 \text{ g/m}^2/\text{month}$). This
493 is similar to the two CO centers at 215 hPa over the tropics (Fig. 16). It is noteworthy that
494 there is a large CO difference between cases where emissions are $0.1 \text{ g/m}^2/\text{month}$ and
495 those with $0.5 \text{ g/m}^2/\text{month}$ emissions over northern Africa, with the latter cases exhibiting
496 larger CO. Over East and South Asia, CO concentration is high in all cases where deep
497 convection is present ($CONV > 1$). Even when emission is weak ($< 0.1 \text{ g/m}^2/\text{month}$), CO
498 mixing ratio can still be high with strong convection, which suggests that CO transport by
499 convection and advection may be important over this region. During the Asian Summer
500 monsoon season, CO emitted from northeast India and southwest China can be
501 transported by deep convection to the UTLS and trapped within the anticyclonic
502 circulation (e.g., Li et al., 2005; Fu et al., 2006). This may account for the high CO over
503 these two regions even though local emission is relatively weak. Over Indonesia, MLS
504 roughly shows two high CO centers, one occurs when both convection and emission are
505 strong (upper right corner) and the other exists when strong emission with weak
506 convection is present (lower right corner).

507 The emission-convection-CO relationships simulated by the two models are quite
508 similar to each other, reflecting their underlying identical meteorology and similar
509 emission inventories. When compared with MLS observation, there is similarity over
510 some regions such as southern Africa, northern Africa and Indonesia. Over other regions,
511 the observed and simulated relationships are quite different. For example, both GMI and



512 GEOS-Chem show two CO centers when convection is strong ($\text{CONV} > 1$) over South
513 America, and they overestimate CO when convection is moderate ($0.1 < \text{CONV} < 1$).
514 Over East Asia, both models overestimate CO when convection is weak or moderate,
515 especially with weak emission ($< 0.2 \text{ g/m}^2/\text{month}$). Over South Asia, both models show a
516 high CO center when both convection and emission are weak (lower left corner), which is
517 not seen in the MLS observation. The emission-convection-CO relationships at 147 hPa
518 over different regions observed by MLS, and the comparisons between observation and
519 model simulations are similar to those at 215 hPa, thus we will not discuss them in detail.

520 **6 Conclusions**

521 In this study, we evaluate the spatial distribution and temporal variation of CO in the
522 upper troposphere and lower stratosphere (UTLS) during 2004–2012 simulated by two
523 chemical transport models (GMI and GEOS-Chem) using the latest version (V4.2) of
524 Aura MLS data. The seasonal and monthly variations of CO, as well as the transport of
525 CO in the UTLS (the “tape recorder”) are compared between MLS observations and
526 model simulations, over both global and regional scales. In addition, the relationships
527 between emission, convection, and CO mixing ratio in the UTLS are investigated over
528 different regions using MLS observations and model simulations.

529 In general, the simulated CO distribution from GMI is quite similar to that from
530 GEOS-Chem at all levels. However, the CO peak values of GEOS-Chem are ~15-20%
531 smaller than GMI at 215 hPa and 147 hPa over South America and Africa during DJF
532 and SON, and ~20% larger than GMI at 100 hPa over South Asia during JJA. Compared
533 with MLS observation, the locations of high CO centers at 215 hPa and 147 hPa are well
534 simulated in GMI and GEOS-Chem, except over Africa. The UTLS transport of CO from



535 East Asia across the Pacific to North America in MAM and JJA is not well simulated by
536 the two models, suggesting perhaps insufficient lofting of polluted continental air masses
537 by warm conveyor belts. In addition, the magnitudes of simulated CO peaks are much
538 smaller than MLS observation, with a maximum underestimation of ~40% at 215 hPa,
539 50–60% at 147 hPa, and ~70% at 100 hPa. For the vertical distribution of zonally
540 averaged CO, the model simulations show more diffuse UT horizontal gradients, stronger
541 vertical gradients below 100 hPa and weaker gradients above 100 hPa than observed by
542 MLS, which may be due to the underestimated upward transport of CO. The two models
543 successfully reproduce the seasonal shift of CO centers in the UT from DJF to JJA, but
544 they fail to simulate a higher CO maximum in the southern subtropics during SON.

545 The high CO concentrations in the northern subtropics are largely underestimated in
546 the models from April to July, especially over South Asia and East Asia. By contrast, the
547 temporal variation of CO in the southern subtropics is well simulated by the models,
548 except that the magnitude is slightly smaller than observed. The high CO values in the
549 UT related to stronger CO emissions generated by drought-induced fires in Indonesia or
550 South America are well captured by GMI during ENSO periods. The semi-annual CO
551 peaks at 100 hPa are not well simulated by the two models, and the peak during MAM is
552 much weaker than the other peak during SON. In general, the observed and simulated CO
553 tape recorders show good agreement over the tropics and southern subtropics. The phase
554 shift and CO anomaly magnitude in the GMI simulation are more consistent with MLS
555 observation than those in the GEOS-Chem simulation. The models show that the location
556 of the tape head is near 200 hPa, which is in rough agreement with MLS data. Over the
557 northern subtropics, CO tape recorders simulated by the models show a 2-3 month time



558 lag between the same phases of CO peak anomaly, which may be caused by an
559 underestimation of vertical transport in the models.

560 On regional scales, the CO concentrations simulated by GMI are generally larger than
561 those from GEOS-Chem, with differences less than 10% at 215 hPa and 147 hPa. The
562 seasonal cycle of CO is similar between MLS and both models over South America,
563 southern Africa and Indonesia, although the magnitude greatly differs. Over three other
564 regions (northern Africa, East Asia, South Asia), the simulated seasonal variation of CO
565 is not consistent with MLS observation. At 100 hPa, GMI is smaller than GEOS-Chem
566 over all regions, especially from May to October. The underestimation of CO by the
567 models reaches its maximum at this level. Vertical CO profile comparisons show that the
568 models underestimate CO at all levels below (i.e., with pressures greater than) 50 hPa
569 observable by MLS, with the magnitude of underestimation depending on region, altitude
570 and season.

571 The relationships between emission, convection and UTLS CO vary with region.
572 Over the tropics, UT CO generally increases with increasing surface emission in the
573 presence of deep convection. When convection is relatively weak, UT CO is generally
574 low and changes little with surface emission. The maximum CO concentration occurs
575 when both convection and emission are strong. GMI and GEOS-Chem simulations
576 generally show similar emission-convection-CO relationships compared with MLS
577 observation at 215 hPa and 147 hPa, except the slope of CO contours have some
578 differences. At 100 hPa, the emission-convection-CO relationships simulated by the two
579 models are quite different from observations. On a regional scale, CO in the UT is
580 generally high when emission and convection are strong, but distinct regional differences



581 also exist, which may be associated with the relative importance of convection and
582 advection in CO transport over different regions. In addition, convection in the tropics
583 and mid-latitudes are fundamentally different, leading to differences in CO transport, and
584 the relative mix of CO from anthropogenic emission, biomass burning, and in-situ
585 production. The simulated emission-convection-CO relationships from GMI and
586 GEOS-Chem are similar to observation over some regions such as southern Africa,
587 northern Africa and Indonesia, but not all regions.

588 Overall, GMI and GEOS-Chem simulations of CO are similar given the same driving
589 meteorology and very similar emission inventories. However, model simulations still
590 show large discrepancies compared with MLS observations, especially in the lower
591 stratosphere, such as at 100 hPa. These discrepancies may be related to the convection
592 parameterization, inaccurate emission inventories, and chemical production and loss rate
593 of CO in the troposphere. More efforts are needed to investigate these factors to improve
594 model simulations in future studies.

595

596 **Appendix A: Comparison of MLS Version 3 and Version 4 CO**

597 Our preliminary comparisons of MLS V3 and V4 CO data have shown that the spatial
598 distributions of CO in the UTLS are quite similar, except for some small differences in
599 the magnitude. In general, CO concentration differences between these two versions are
600 within 20%. The seasonal CO peak values of V4 are slightly larger than V3 at 215 hPa
601 and 147 hPa, but become smaller than V3 at 100 hPa. The maximum differences is ~12–
602 17% for different seasons.



603 The improvements of MLS V4 compared with V3 CO can be seen in the vertical
604 distribution of zonal mean CO (Fig. A1) and the vertical CO profiles (Fig. A2). One
605 improvement is that the cloud contamination is significantly reduced, the other is the
606 more realistic CO gradient from 215 hPa to 100 hPa. In order to better illustrate the
607 differences between different versions, we also add the CO measurements from the
608 Atmospheric Chemistry Experiment - Fourier Transform Spectrometer (ACE-FTS)
609 (Bernath et al., 2005). This instrument is on board the Canadian satellite SCISAT-1,
610 operating between 750 and 4400 cm^{-1} with a high spectral-resolution (0.02 cm^{-1}) and
611 using a solar occultation observation technique. ACE-FTS observations are used to derive
612 volume mixing ratio profiles of over 30 atmospheric trace gases (Boone et al., 2005),
613 measuring each spacecraft sunrise and sunset (~30 profiles per day compared to ~3500
614 for Aura MLS). It has been providing consistent measurements since February 2004. The
615 atmospheric profiles provided by ACE-FTS range in altitude of ~5–110 km depending on
616 the species, with a vertical resolution of ~3–4 km. The data used are ACE-FTS Level 2
617 Version 3.5 (V3.5) (Boone et al., 2013) with the same period as MLS data (August 2004
618 – December 2012).

619 The vertical distribution of zonal mean CO in the pressure-latitude cross-section and
620 its seasonal variations as observed by MLS and ACE-FTS are shown in Figure A1.
621 During boreal Winter (DJF), MLS V3 CO shows a decrease between 160 hPa and 130
622 hPa, which may be caused by cloud contamination. This abnormal gap does not exist in
623 MLS V4 and ACE-FTS CO observation. Such improvement is also shown during MAM.
624 In addition, the magnitude of high CO centers in MLS V4 is higher than that in MLS V3
625 and has better agreement with ACE-FTS measurement. The tropical average (30 °S–30 °N)



626 of CO vertical profile in the UTLS and its seasonal variation as observed by MLS and
627 ACE-FTS are shown in Figure A2. Compared with MLS V3 data, V4 CO is more
628 realistic in the CO gradient from 215 hPa to 100 hPa. For example, MLS V3 data show
629 that CO decreases from 215 hPa to 147 hPa and then increases from 147 hPa to 100 hPa
630 during DJF season, but V4 data show that it monotonically decreases from 215 hPa to
631 100 hPa, which is consistent with ACE-FTS CO observation. This improvement is also
632 found in regional analysis (e.g., Indonesia). Furthermore, MLS V4 CO also shows better
633 agreement with ACE-FTS CO than V3 CO during other seasons.

634

635 **Acknowledgements**

636 This research is supported by the NASA AST program. The study was performed at
637 NASA Jet Propulsion Laboratory (JPL) at the California Institute of Technology, under
638 contract with NASA. The first author would like to thank Dr. William G. Read for help
639 with the application of MLS averaging kernels to model simulations.

640

641 **References**

- 642 Alexander, B., Savarino, J., Lee, C. C. W., Park, R. J., Jacob, D. J., Thiemens, M. H., Li,
643 Q. B., and Yantosca, R. M.: Sulfate formation in sea-salt aerosols: Constraints from
644 oxygen isotopes, *J. Geophys. Res.*, 110, D10307, doi:10.1029/2004JD005659, 2005.
- 645 Barkley, M., P. Palmer, L. Ganzeveld, A. Arneth, D. Hagberg, T. Karl, A. Guenther, F.
646 Paulot, P. Wennberg, J. Mao, T. Kurosu, K. Chance, J.-F. Muller, I. De Smedt, M. Van
647 Roozendaal, D. Chen, Y. Wang, and R. Yantosca: Can a “state of the art” chemistry



- 648 transport model simulate Amazonian tropospheric chemistry? , J. Geophys. Res., 116,
649 D16302, doi:10.1029/2011JD015893, 2011.
- 650 Bernath, P. F., McElroy, C. T., Abrams, M. C., Boone, C. D., Butler, M., Camy-Peyret,
651 C., Carleer, M., Clerbaux, C., Coheur, P.-F., Colin, R., DeCola, P., DeMazière, M.,
652 Drummond, J. R., Dufour, D., Evans, W. F. J., Fast, H., Fussen, D., Gilbert, K.,
653 Jennings, D. E., Llewellyn, E. J., Lowe, R. P., Mahieu, E., McConnell, J. C., McHugh,
654 M., McLeod, S. D., Michaud, R., Midwinter, C., Nassar, R., Nichitiu, F., Nowlan, C.,
655 Rinsland, C. P., Rochon, Y. J., Rowlands, N., Semeniuk, K., Simon, P., Skelton, R.,
656 Sloan, J. J., Soucy, M.-A., Strong, K., Tremblay, P., Turnbull, D., Walker, K.
657 A., Walkty, I., Wardle, D. A., Wehrle, V., Zander, R., and Zou, J.: Atmospheric
658 Chemistry Experiment (ACE): Mission overview, Geophys. Res. Lett., 32, L15S01,
659 doi:10.1029/2005GL022386, 2005.
- 660 Bey, I., Aumont, B., and Toupance, G.: A modeling study of the nighttime radical
661 chemistry in the lower continental troposphere: 1. Development of a detailed chemical
662 mechanism including nighttime chemistry, J. Geophys. Res., 106(D9), 9959–9990,
663 doi:10.1029/2000JD900347, 2001a.
- 664 Bey, I., Jacob, D. J., Yantosca, R. M., Logan, J. A., Field, B. D., Fiore, A. M., Li, Q. B.,
665 Liu, H. G. Y., Mickley, L. J., and Schultz, M. G.: Global modeling of tropospheric
666 chemistry with assimilated meteorology: Model description and evaluation, J. Geophys.
667 Res., 106, 23073–23096, 2001b.
- 668 Bian, H., and Prather, M. J.: Fast-J2: Accurate Simulation of stratospheric photolysis in
669 global chemical models, J. Atmos. Chem., 41, 281–296, 2002.



- 670 Boone, C. D., Nassar, R., Walker, K. A., Rochon, Y., McLeod, S. D., Rinsland, C. P., and
671 Bernath, P. F.: Retrievals for the Atmospheric Chemistry Experiment
672 Fourier-Transform Spectrometer, *Appl. Optics*, 44, 7218–7231,
673 doi:10.1364/AO.44.007218, 2005.
- 674 Boone, C. D., Walker, K. A., and Bernath, P. F.: Version 3 Retrievals for the
675 Atmospheric Chemistry Experiment Fourier Transform Spectrometer (ACE-FTS), The
676 Atmospheric Chemistry Experiment ACE at 10: A Solar Occultation Anthology, A.
677 Deepak Publishing, Hampton, Virginia, USA, 103–127, 2013.
- 678 Brewer, A. W.: Evidence for a World Circulation Provided by the Measurements of
679 Helium and Water Vapour Distribution in the Stratosphere, *Q. J. Roy. Meteor. Soc.*, 75,
680 351–363, 1949.
- 681 Daniel, J. S., and Solomon, S.: On the climate forcing of carbon monoxide, *J. Geophys.*
682 *Res.*, 103, 13249–13260, 1998.
- 683 De Laat, A., Gloudemans, A., Aben, I., Krol, M., Meirink, J., van der Werf, G., and
684 Schrijver, H.: SCIAMACHY carbon monoxide total columns: statistical evaluation and
685 comparison with CTM results, *J. Geophys. Res.*, 112, D12310,
686 doi:10.1029/2006JD008256, 2007.
- 687 Duncan, B. N., Strahan, S. E., Yoshida, Y., Steenrod, S. D., and Livesey, N.: Model study
688 of the cross-tropopause transport of biomass burning pollution, *Atmos. Chem. Phys.*, 7,
689 3713–3736, doi:10.5194/acp-7-3713-2007, 2007.
- 690 Edwards, D. P., Emmons, L. K., Gille, J. C., Chu, A., Attie, J. L., Giglio, L., Wood, S. W.,
691 Haywood, J., Deeter, M. N., Massie, S. T., Ziskin, D. C., and Drummond, J. R.:



- 692 Satellite-observed pollution from Southern Hemisphere biomass burning, *J. Geophys.*
693 *Res.*, 111, D14312, doi:10.1029/2005JD006655, 2006.
- 694 Fu, R., Hu, Y. L., Wright, J. S., Jiang, J. H., Dickinson, R. E., Chen, M. X., Filipiak, M.,
695 Read, W. G., Waters, J. W., and Wu, D. L.: Short circuit of water vapor and polluted
696 air to the global stratosphere by convective transport over the Tibetan Plateau, *P. Natl.*
697 *Acad. Sci. USA*, 103, 5664–5669, doi:10.1073/pnas.0601584103, 2006.
- 698 Gloudemans, A., Krol, M., Meirink, J., De Laat, A., Van der Werf, G., Schrijver, H., Van
699 den Broek, M., and Aben, I.: Evidence for long-range transport of carbon monoxide in
700 the Southern Hemisphere from SCIAMACHY observations, *Geophys. Res. Lett.*, 33,
701 L16807, doi:10.1029/2006GL026804, 2006.
- 702 Gonzi, S., and Palmer, P. I.: Vertical transport of surface fire emissions observed from
703 space, *J. Geophys. Res.*, 115, D02306, doi:10.1029/2009JD012053, 2010.
- 704 Guenther, A., Karl, T., Harley, P., Wiedinmyer, C., Palmer, P. I., and Geron, C.:
705 Estimates of global terrestrial isoprene emissions using MEGAN (Model of Emissions
706 of Gases and Aerosols from Nature), *Atmos. Chem. Phys.*, 6, 3181–3210,
707 doi:10.5194/acp-6-3181-2006, 2006.
- 708 Heald, C. L., D. J. Jacob, D. B. A. Jones, P. I. Palmer, J. A. Logan, D. G. Streets, G. W.
709 Sachse, J. C. Gille, R. N. Hoffman, and T. Nehr Korn: Comparative inverse analysis of
710 satellite (MOPITT) and aircraft (TRACE-P) observations to estimate Asian sources of
711 carbon monoxide, *J. Geophys. Res.*, 109, D23306, doi:10.1029/2004JD005185, 2004.
- 712 Huang, L., Fu, R., Jiang, J. H., Wright, J. S., and Luo, M.: Geographic and seasonal
713 distributions of CO transport pathways and their roles in determining CO centers in the



- 714 upper troposphere, Atmos. Chem. Phys., 12, 4683–4698,
715 doi:10.5194/acp-12-4683-2012, 2012.
- 716 Huang, L., Fu, R., and Jiang, J. H.: Impacts of fire emissions and transport pathways on
717 the interannual variation of CO in the tropical upper troposphere, Atmos. Chem. Phys.,
718 14, 4087-4099, doi:10.5194/acp-14-4087-2014, 2014.
- 719 Hudman, R. C., et al.: Surface and lightning sources of nitrogen oxides over the United
720 States: Magnitudes, chemical evolution, and outflow, J. Geophys. Res., 112, D12S05,
721 doi:10.1029/2006JD007912, 2007
- 722 Jacob, D. J., Introduction to Atmospheric Chemistry, Princeton University Press,
723 Princeton, New Jersey, USA, 1999.
- 724 Jiang, J. H., Livesey, N. J., Su, H., Neary, L., McConnell, J. C., and Richards, N. A. D.:
725 Connecting surface emissions, convective uplifting, and long-range transport of carbon
726 monoxide in the upper troposphere: New observations from the Aura Microwave Limb
727 Sounder, Geophys Res Lett, 34, Doi 10.1029/2007gl030638, 2007.
- 728 Jiang, J. H., Su, H., Zhai, C., Massie, S. T., Schoeberl, M. R., Colarco, P. R., Platnick, S.,
729 Gu, Y., and Liou, K.-N.: Influence of convection and aerosol pollution on ice cloud
730 particle effective radius, Atmos. Chem. Phys., 11, 457–463, doi:
731 10.5194/acp-11-457-2011, 2011.
- 732 Kopacz, M., D. J. Jacob, D. Henze, C. L. Heald, D. G. Streets, and Q. Zhang:
733 Comparison of adjoint and analytical Bayesian inversion methods for constraining
734 Asian sources of carbon monoxide using satellite (MOPITT) measurements of CO
735 columns, J. Geophys. Res., 114, D04305, doi:10.1029/2007JD009264, 2009.



- 736 Kopacz, M., Jacob, D. J., Fisher, J. A., Logan, J. A., Zhang, L., Megretskaia, I. A.,
737 Yantosca, R. M., Singh, K., Henze, D. K., Burrows, J. P., Buchwitz, M., Khlystova, I.,
738 McMillan, W. W., Gille, J. C., Edwards, D. P., Eldering, A., Thouret, V., and Nedelec,
739 P.: Global estimates of CO sources with high resolution by adjoint inversion of
740 multiple satellite datasets (MOPITT, AIRS, SCIAMACHY, TES), Atmos. Chem.
741 Phys., 10, 855-876, doi:10.5194/acp-10-855-2010, 2010.
- 742 Li, Q. B., Jiang, J. H., Wu, D. L., Read, W. G., Livesey, N. J., Waters, J. W., Zhang, Y. S.,
743 Wang, B., Filipiak, M. J., Davis, C. P., Turquety, S., Wu, S. L., Park, R. J., Yantosca,
744 R. M., and Jacob, D. J.: Convective outflow of South Asian pollution: A global CTM
745 simulation compared with EOS MLS observations, Geophys. Res. Lett., 32, L14826,
746 doi:10.1029/2005GL022762, 2005.
- 747 Liu, C. T., Zipser, E., Garrett, T., Jiang, J. H., and Su, H.: How do the water vapor and
748 carbon monoxide “tape recorders” start near the tropical tropopause?, Geophys Res
749 Lett, 34, doi: 10.1029/2006gl029234, 2007.
- 750 Liu, J., Logan, J. A., Jones, D. B. A., Livesey, N. J., Megretskaia, I., Carouge, C., and
751 Nedelec, P.: Analysis of CO in the tropical troposphere using Aura satellite data and
752 the GEOS-Chem model: insights into transport characteristics of the GEOS
753 meteorological products, Atmos Chem Phys, 10, 12207-12232, DOI
754 10.5194/acp-10-12207-2010, 2010.
- 755 Liu, J., Logan, J. A., Murray, L. T., Pumphrey, H. C., Schwartz, M. J., and
756 Megretskaia, I. A.: Transport analysis and source attribution of seasonal and
757 interannual variability of CO in the tropical upper troposphere and lower stratosphere,
758 Atmos. Chem. Phys., 13, 129–146, doi: 10.5194/acp-13-129-2013, 2013.



- 759 Livesey, N. J., Filipiak, M. J., Froidevaux, L., Read, W. G., Lambert, A., Santee, M. L.,
760 Jiang, J. H., Pumphrey, H. C., Waters, J. W., Cofield, R. E., Cuddy, D. T., Daffer, W.
761 H., Drouin, B. J., Fuller, R. A., Jarnot, R. F., Jiang, Y. B., Knosp, B. W., Li, Q. B.,
762 Perun, V. S., Schwartz, M. J., Snyder, W. V., Stek, P. C., Thurstans, R. P., Wagner, P.
763 A., Avery, M., Browell, E. V., Cammas, J. P., Christensen, L. E., Diskin, G. S., Gao, R.
764 S., Jost, H. J., Loewenstein, M., Lopez, J. D., Nedelec, P., Osterman, G. B., Sachse, G.
765 W., and Webster, C. R.: Validation of Aura Microwave Limb Sounder O-3 and CO
766 observations in the upper troposphere and lower stratosphere, *J Geophys Res-Atmos*,
767 113, Doi 10.1029/2007jd008805, 2008.
- 768 Livesey, N. J., Read, W. G., Froidevaux, L., Lambert, A., Manney, G. L.: EOS MLS
769 version 3.3 Level 2 data quality and description document, Jet Propulsion Laboratory,
770 California Institute of Technology, Pasadena, CA, 2011.
- 771 Livesey, N. J., Logan, J. A., Santee, M. L., Waters, J. W., Doherty, R. M., Read, W. G.,
772 Froidevaux, L., and Jiang, J. H.: Interrelated variations of O₃, CO and deep convection
773 in the tropical/subtropical upper troposphere observed by the Aura Microwave Limb
774 Sounder (MLS) during 2004–2011, *Atmos. Chem. Phys.*, 13, 579–598,
775 doi:10.5194/acp-13-579-2013, 2013.
- 776 Livesey, N. J., Read, W. G., Wagner, P. A., Froidevaux, L., Lambert, A., Manney, G. L.,
777 Millán, L., Pumphrey, H. C., Santee, M. L., Schwartz, M. J., Wang, S., Fuller, R. A.,
778 Jarnot, R. F., Knosp, B. W., and Martinez, E.: EOS MLS Version 4.2x Level 2 data
779 quality and description document, Jet Propulsion Laboratory, California Institute of
780 Technology, Pasadena, CA, 2015.



- 781 Logan, J. A., Prather, M. J., Wofsy, S. C., and McElroy, M. B.: Tropospheric chemistry:
782 A global perspective, *J. Geophys. Res.*, 86, 7210–7254, 1981.
- 783 Mote, P. W., Rosenlof, K. H., Holton, J. R., Harwood, R. S., and Waters, J. W.: Seasonal
784 variations of water vapor in the tropical lower stratosphere, *Geophys. Res. Lett.*, 22,
785 1093–1096, 1995.
- 786 Murray, L. T., Logan, J. A., and Jacob, D. J.: Interannual variability in tropical
787 tropospheric ozone and OH: the role of lightning, *J. Geophys. Res.*, 118, 11468–11480,
788 doi:10.1002/jgrd.50857, 2013.
- 789 Park, R. J., Jacob, D. J., Chin, M., and Martin, R. V.: Sources of carbonaceous aerosols
790 over the United States and implications for natural visibility, *J. Geophys. Res.*, 108,
791 4355, doi:10.1029/2002JD003190, 2003.
- 792 Ricaud, P., Barret, B., Attié J.-L., Motte, E., Le Flochmoën, E., Teyssède, H., Peuch,
793 V.-H., Livesey, N., Lambert, A., and Pommereau, J.-P.: Impact of land convection on
794 troposphere-stratosphere exchange in the tropics, *Atmos. Chem. Phys.*, 7, 5639–5657,
795 doi:10.5194/acp-7-5639-2007, 2007.
- 796 Rienecker, M. M., Suarez, M. J., Gelaro, R., Todling, R., Bacmeister, J., Liu, E.,
797 Bosilovich, M. G., Schubert, S. D., Takacs, L., Kim, G.-K., Bloom, S., Chen, J.,
798 Collins, D., Conaty, A., da Silva, A., Gu, W., Joiner, J., Koster, R. D., Lucchesi, R.,
799 Molod, A., Owens, T., Pawson, S., Pegion, P., Redder, C. R., Reichle, R., Robertson, F.
800 R., Ruddick, A. G., Sienkiewicz, M., and Woollen, J.: MERRA: NASA's Modern-Era
801 Retrospective Analysis for Research and Applications, *J. Climate*, 24, 3624–3648,
802 doi:10.1175/JCLI-D-11-00015.1, 2011.



803 Rotman, D. A., Tannahill J. R., Kinnison D. E., Connell, P. S., Bergmann, D., Proctor, D.,
804 Rodriguez, J. M., Lin, S. J., Rood, R. B., Prather, M. J., Rasch, P. J., Considine, D. B.,
805 Ramarosan, R., and Kawa, S. R.: Global Modeling Initiative assessment model: Model
806 description, integration, and testing of the transport shell, *J. Geophys. Res.*, 106(D2),
807 1669–1691, doi:10.1029/2000JD900463, 2001.

808 Schoeberl, M. R., Duncan, B. N., Douglass, A. R., Waters, J., Livesey, N., Read, W., and
809 Filipiak, M.: The carbon monoxide tape recorder, *Geophys. Res. Lett.*, 33, doi:
810 10.1029/2006gl026178, 2006.

811 Schultz, M., Rast, S., van het Bolscher, M., Pulles, T., Brand, R., Pereira, J., Mota, B.,
812 Spessa, A., Dalsøren, S., van Noije, T., and Szopa, S.: Emission data sets and
813 methodologies for estimating emissions, RETRO project report D1-6, Hamburg,
814 available at: http://retro.enes.org/reports/D1-6_final.pdf, 26 February 2007.

815 Shindell, D., Faluvegi, G., Stevenson, D., Krol, M., Emmons, L., Lamarque, J.-F., Petron,
816 G., Dentener, F., Ellingsen, K., Schultz, M., Wild, O., Amann, M., Atherton, C. S.,
817 Bergmann, D. J., Bey, I., Butler, T., Cofala, J., Collins, W. J., Derwent, R. G., Doherty,
818 R. M., Drevet, J., Eskes, H. J., Fiore, A. M., Gauss, M., Hauglustaine, D. A., Horowitz,
819 L. W., Isaksen, I. S. A., Lawrence, M. G., Montanaro, V., Müller, J.-F., Pitari, G.,
820 Prather, M. J., Pyle, J. A., Rast, S., Rodriguez, J. M., Sanderson, M. G., Savage, N. H.,
821 Strahan, S. E., Sudo, K., Szopa, S., Unger, N., van Noije, T. P. C., and Zeng, G.:
822 Multimodel simulations of carbon monoxide: Comparison with observations and
823 projected near-future changes, *J. Geophys. Res.*, 111, D19306,
824 doi:10.1029/2006JD007100, 2006.



- 825 van der Werf, G. R., Randerson, J. T., Giglio, L., Collatz, G., Mu, M., Kasibhatla, P. S.,
826 Morton, D. C., DeFries, R., Jin, Y., and van Leeuwen, T. T.: Global fire emissions and
827 the contribution of deforestation, savanna, forest, agricultural, and peat fires (1997–
828 2009), *Atmos. Chem. Phys.*, 10, 11,707–711,735, 2010.
- 829 van Donkelaar, A., Martin, R. V., Leaitch, W. R., Macdonald, A. M., Walker, T. W.,
830 Streets, D. G., Zhang, Q., Dunlea, E. J., Jimenez, J. L., Dibb, J. E., Huey, L. G., Weber,
831 R., and Andreae, M. O.: Analysis of aircraft and satellite measurements from the
832 Intercontinental Chemical Transport Experiment (INTEX-B) to quantify long-range
833 transport of East Asian sulfur to Canada, *Atmos. Chem. Phys.*, 8, 2999-3014,
834 doi:10.5194/acp-8-2999-2008, 2008.
- 835 Waters, J.W., Froidevaux, L., Harwood, R. S., Jarnot, R. F., Pickett, H. M., Read, W. G.,
836 Siegel, P. H., Cofield, R. E., Filipiak, M. J., Flower, D. A., Holden, J. R., Lau, G. K.,
837 Livesey, N. J., Manney, G. L., Pumphrey, H. C., Santee, M. L., Wu, D. L., Cuddy, D.
838 T., Lay, R. R., Loo, M. S., Perun, V. S., Schwartz, M. J., Stek, P. C., Thurstans, R. P.,
839 Chandra, K. M., Chavez, M. C., Chen, G., Boyles, M. A., Chudasama, B. V., Dodge,
840 R., Fuller, R. A., Girard, M. A., Jiang, J. H., Jiang, Y., Knosp, B. W., LaBelle, R. C.,
841 Lam, J. C., Lee, K. A., Miller, D., Oswald, J. E., Patel, N. C., Pukala, D. M., Quintero,
842 O., Scaff, D. M., Snyder, W. V., Tope, M. C., Wagner, P. A., and Walch, M. J.: The
843 Earth Observing System Microwave Limb Sounder (EOS MLS) on the Aura satellite,
844 *IEEE Trans. Geosci. Remote Sens.*, 44, 1075–1092, 2006.
- 845 Wild, O., Zhu, X., and Prather, M.: Fast-J: Accurate simulation of in- and below- cloud
846 photolysis in tropospheric chemical models, *J. Atmos. Chem.*, 37, 245–282, 2000.



- 847 Wu, D. L., Jiang, J. H., Read, W. G., Austin, R. T., David, C. P., Lambert, A., Stephens,
848 G. L., Vane, D. G., and Waters, J. W.: Validation of Aura MLS cloud Ice Water
849 Content (IWC) measurements, *J. Geophys. Res.*, 113, D15S10,
850 doi:10.1029/2007LD008931, 2008.
- 851 Wu, S., L. J. Mickley, D. J. Jacob, J. A. Logan, R. M. Yantosca, and D. Rind: Why are
852 there large differences between models in global budgets of tropospheric ozone? *J.*
853 *Geophys. Res.*, 112, D05302, doi:10.1029/2006JD007801, 2007.
- 854 Xiao, Y., J. A. Logan, D. J. Jacob, R. C. Hudman, R. Yantosca, and D. R. Blake: Global
855 budget of ethane and regional constraints on U.S. sources, *J. Geophys. Res.*, 113,
856 D21306, doi:10.1029/2007JD009415, 2008.
- 857 Yevich, R., and Logan, J. A.: An assessment of biofuel use and burning of agricultural
858 waste in the developing world, *Global Biogeochem. Cycles*, 17, 1095,
859 doi:10.1029/2002GB001952, 2003.
- 860 Zhang, G. J., and McFarlane, N. A.: Sensitivity of climate simulations to the
861 parameterization of cumulus convection in the Canadian Climate Centre general
862 circulation model, *Atmos. Ocean.*, 33, 407–446, 1995.
- 863 Zhang, Q., Streets, D. G., Carmichael, G. R., He, K. B., Huo, H., Kannari, A., Klimont,
864 Z., Park, I. S., Reddy, S., Fu, J. S., Chen, D., Duan, L., Lei, Y., Wang, L. T., and Yao,
865 Z. L.: Asian emissions in 2006 for the NASA INTEX-B mission, *Atmos. Chem. Phys.*,
866 9, 5131–5153, doi:10.5194/acp-9-5131-2009, 2009.
- 867

868 **Table Captions**

869 **Table 1.** Annual mean and interannual standard deviation of CO budgets (biofuel and
870 fossil fuel emissions, biomass burning emissions, tropospheric chemical production,



871 tropospheric methane oxidation, loss with tropospheric OH, and net transport from
872 troposphere to stratosphere) for GMI and GEOS-Chem during 2004 – 2012 (units in
873 Tmol/year).

874 **Table 2.** Statistical comparison of model-simulated and MLS-observed (V4) CO at (a)
875 215 hPa, (b) 147 hPa, and (c) 100 hPa during each season.

876

877 **Figure Captions**

878 **Fig. 1.** Seasonal mean (DJF, MAM, JJA, and SON) distribution of CO mixing ratio at
879 215 hPa for December 2004 – November 2012 from: (top row) MLS V4 data; (middle
880 row) GMI model simulation with MLS averaging kernels (AKs) applied; (bottom row)
881 GEOS-Chem model simulation with MLS AKs applied.

882 **Fig. 2.** As in Fig. 1, but for CO mixing ratio at 147 hPa.

883 **Fig. 3.** As in Fig. 1, but for CO mixing ratio at 100 hPa.

884 **Fig. 4.** Vertical/latitudinal distribution of zonal mean CO mixing ratio during different
885 seasons (DJF, MAM, JJA, and SON) from: (top row) MLS V4 data; (middle row) GMI
886 model simulation with MLS AKs applied; (bottom row) GEOS-Chem model simulation
887 with MLS AKs applied.

888 **Fig. 5.** Monthly variation of zonal mean CO mixing ratio at 215 hPa for August 2004 –
889 December 2012 from: (top row) MLS V4 data; (middle row) GMI model simulation with
890 MLS AKs applied; (bottom row) GEOS-Chem model simulation with MLS AKs applied.

891 **Fig. 6.** As in Fig. 5, but for CO mixing ratio at 100 hPa.

892 **Fig. 7.** Monthly variation of meridional mean (15°S–15°N) CO mixing ratio at 215 hPa
893 for August 2004 – December 2012 from: (left) MLS V4 data; (middle) GMI model



894 simulation with MLS AKs applied; (right) GEOS-Chem model simulation with MLS
895 AKs applied.

896 **Fig. 8.** As in Fig. 7, but for CO mixing ratio at 100 hPa.

897 **Fig. 9.** Temporal variation of monthly mean CO deviations, zonally averaged over the
898 tropics (15°S–15°N), vertically from 200 hPa to 50 hPa for August 2004 – December
899 2012 from (top row) MLS V4 data; (middle row) GMI model simulation with MLS AKs
900 applied; (bottom row) GEOS-Chem model simulation with MLS AKs applied. An 8-year
901 mean (2005–2012) was subtracted from the monthly mean time series at each level for
902 MLS data and the two models' simulations.

903 **Fig. 10.** As in Fig. 9, but over the northern subtropics (10°–30°N).

904 **Fig. 11.** As in Fig. 9, but over the southern subtropics (10°–30°S).

905 **Fig. 12.** Climatological (8-year) monthly mean of CO mixing ratio at 215 hPa from MLS
906 V4 data (black line), GMI model simulation with MLS AKs applied (red line), and
907 GEOS-Chem model simulation with MLS AKs applied (blue line) over the selected six
908 regions: (a) South America, (b) Southern Africa, (c) Northern Africa, (d) East Asia, (e)
909 South Asia, and (f) Indonesia. The error bars indicate ± 1 interannual standard deviation
910 of the monthly mean CO from MLS V4 data.

911 **Fig. 13.** As in Fig. 12, but for CO mixing ratio at 100 hPa.

912 **Fig. 14.** Climatological (8-year) seasonal mean vertical profile of CO mixing ratio from
913 MLS V4 data (black line), GMI model simulation with MLS AKs applied (red line), and
914 GEOS-Chem model simulation with MLS AKs applied (blue line) over the selected six
915 regions: (top row) South America, (second row from top) Southern Africa, (third row



916 from top) Northern Africa, (fourth row from top) East Asia, (fifth row from top) South
917 Asia, and (bottom row) Indonesia.

918 **Fig. 15.** Climatological monthly mean of surface CO emission from GMI model (red
919 line), ice water content (blue line) and CO mixing ratio (black line) at 215 hPa (left
920 column), 147 hPa (middle column), and 100 hPa (left column) from MLS observation
921 over six regions: (top row) South America, (second row from top) Southern Africa, (third
922 row from top) Northern Africa, (fourth row from top) East Asia, (fifth row from top)
923 South Asia, and (bottom row) Indonesia. Each variable is normalized for comparison.

924 **Fig. 16.** Contour plots of normalized CO mixing ratio at 215 hPa (top row) and 147 hPa
925 (bottom row) over the tropics (30 °S–30 °N) from MLS observation (left column), GMI
926 model simulation (middle column), and GEOS-Chem model simulation (left column)
927 binned according to the surface CO emission (x-axis) and convective index (y-axis) at the
928 same pressure level. See text for more details.

929 **Fig. 17.** Contour plots of normalized CO mixing ratio at 215 hPa over six regions: (top
930 row) South America, (second row from top) Southern Africa, (third row from top)
931 Northern Africa, (fourth row from top) East Asia, (fifth row from top) South Asia, and
932 (bottom row) Indonesia, from MLS observation (left column), GMI model simulation
933 (middle column), and GEOS-Chem model simulation (left column) binned according to
934 the surface CO emission (x-axis) and convective index (y-axis) at the same pressure level.
935 See text for more details.

936 **Fig. A1.** Vertical distribution of zonal mean CO mixing ratio in the pressure-latitude
937 cross-section during different seasons (DJF, MAM, JJA, and SON) from: (top row) MLS



938 Version 3 CO data; (middle row) MLS Version 4 CO data; (bottom row) ACE-FTS CO
939 data with MLS averaging kernels (AKs) applied.

940 **Fig. A2.** Climatological (8-year) seasonal mean vertical profile of CO mixing ratio from
941 MLS Version 4 CO data (black line), MLS Version 3 CO data (gray line), and ACE-FTS
942 CO data with MLS AKs applied (red line) over the tropics (30 °S–30 °N).

943

944 **Tables**

945 **Table 1.** Annual mean and interannual standard deviation of CO budgets (biofuel and
946 fossil fuel emissions, biomass burning emissions, tropospheric chemical production,
947 tropospheric methane oxidation, loss with tropospheric OH, and net transport from
948 troposphere to stratosphere) for GMI and GEOS-Chem during 2004 – 2012 (units in
949 Tmol/year).

Model	GMI	GEOS-Chem
biofuel + fossil fuel	20.6 ± 0.16	19.6 ± 0.29
biomass burning	11.9 ± 1.9	11.9 ± 2.0
tropospheric chemical production	42.3 ± 0.92	59.1 ± 0.77
tropospheric CH ₄ oxidation	30.3 ± 0.95	35.2 ± 0.42
loss with tropospheric OH	77.7 ± 2.1	89.1 ± 2.4
net transport to stratosphere	1.37 ± 0.49	1.50 ± 0.47

950

951 **Table 2.** Statistical comparison of model-simulated and MLS-observed (V4) CO at (a)
952 215 hPa, (b) 147 hPa, and (c) 100 hPa during each season.

953

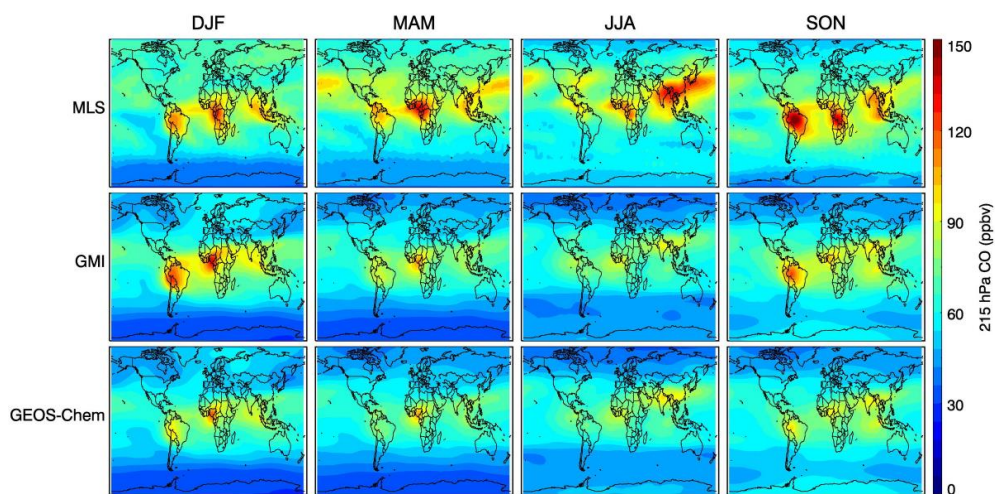


Level	Season	Correlation			Minimum (%)			Maximum (%)			Mean (%)		
		GMI vs V4	GEOS vs V4	GMI vs GEOS	GMI-V 4	GEOS-V 4	GEOS - GMI	GMI-V 4	GEOS-V 4	GEOS - GMI	GMI-V 4	GEOS-V 4	GEOS - GMI
(a) 215 hPa	DJF	0.89	0.90	0.990	-39.0	-40.8	-21.4	30.7	14.5	3.2	-10.5	-16.6	-6.8
	MAM	0.90	0.90	0.995	-36.6	-37.9	-12.1	7.50	4.1	4.1	-20.0	-22.1	-2.7
	JJA	0.83	0.85	0.993	-40.3	-39.9	-6.8	13.7	9.9	8.9	-20.2	-19.5	0.8
	SON	0.85	0.82	0.983	-43.5	-47.9	-19.9	44.3	45.1	4.3	-11.1	-14.5	-3.8
(b) 147 hPa	DJF	0.92	0.93	0.996	-61.7	-60.0	-17.4	6.4	-2.1	5.6	-27.5	-29.1	-2.2
	MAM	0.96	0.95	0.998	-59.7	-59.2	-7.0	-6.6	-5.5	6.5	-32.4	-31.5	1.3
	JJA	0.96	0.97	0.997	-53.8	-52.0	-1.9	-4.4	-5.6	15.6	-31.3	-27.8	5.2
	SON	0.96	0.96	0.996	-50.0	-47.9	-13.7	5.0	6.2	10.3	-25.2	-24.1	1.4
(c) 100 hPa	DJF	0.93	0.94	0.999	-70.2	-68.4	-3.2	-21.9	-21.9	8.4	-46.1	-43.9	4.0
	MAM	0.97	0.97	0.999	-64.1	-63.0	1.0	-29.8	-27.1	10.0	-47.8	-44.8	5.6
	JJA	0.92	0.93	0.998	-67.9	-66.4	1.4	-23.7	-18.6	20.1	-47.4	-42.8	8.7
	SON	0.97	0.97	0.997	-61.7	-60.0	-0.6	-22.0	-18.0	14.6	-44.7	-40.6	7.5

954

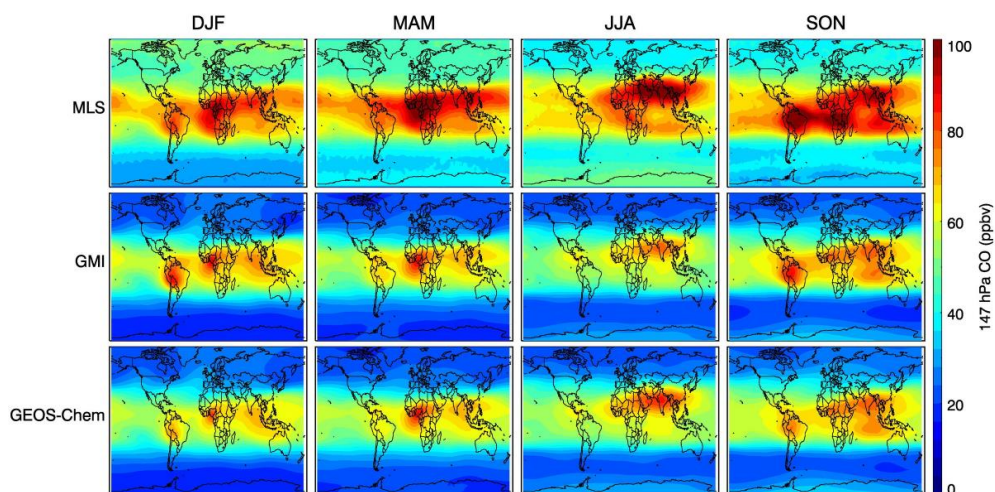


955 **Figures**



956

957 **Fig. 1.** Seasonal mean (DJF, MAM, JJA, and SON) distribution of CO mixing ratio at
958 215 hPa for December 2004 – November 2012 from: (top row) MLS V4 data; (middle
959 row) GMI model simulation with MLS averaging kernels (AKs) applied; (bottom row)
960 GEOS-Chem model simulation with MLS AKs applied.

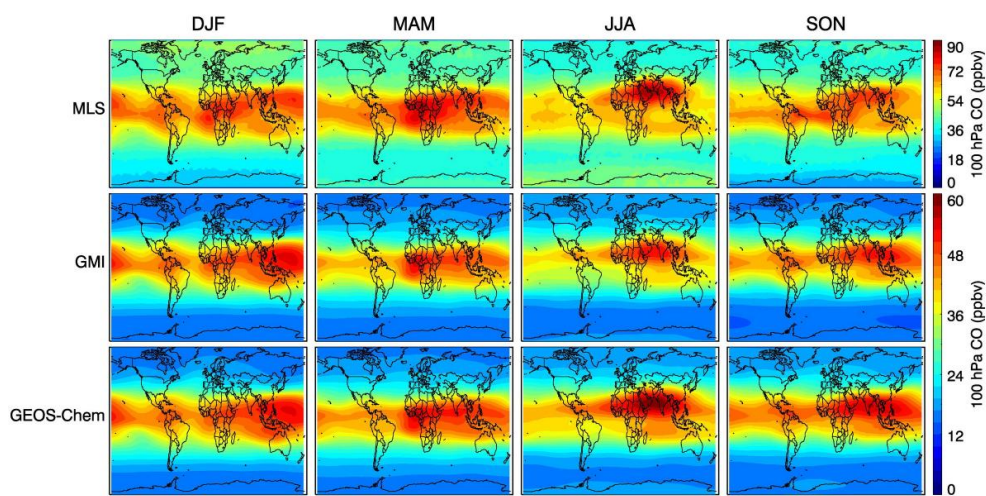


961

962 **Fig. 2.** As in Fig. 1, but for CO mixing ratio at 147 hPa.



963



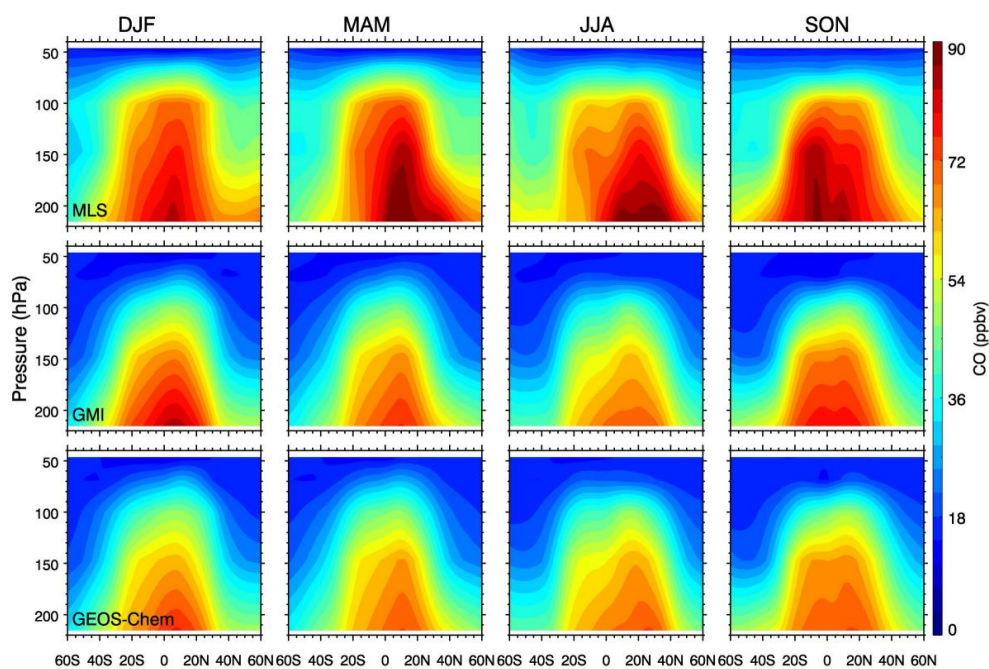
964

965 **Fig. 3.** As in Fig. 1, but for CO mixing ratio at 100 hPa.

966

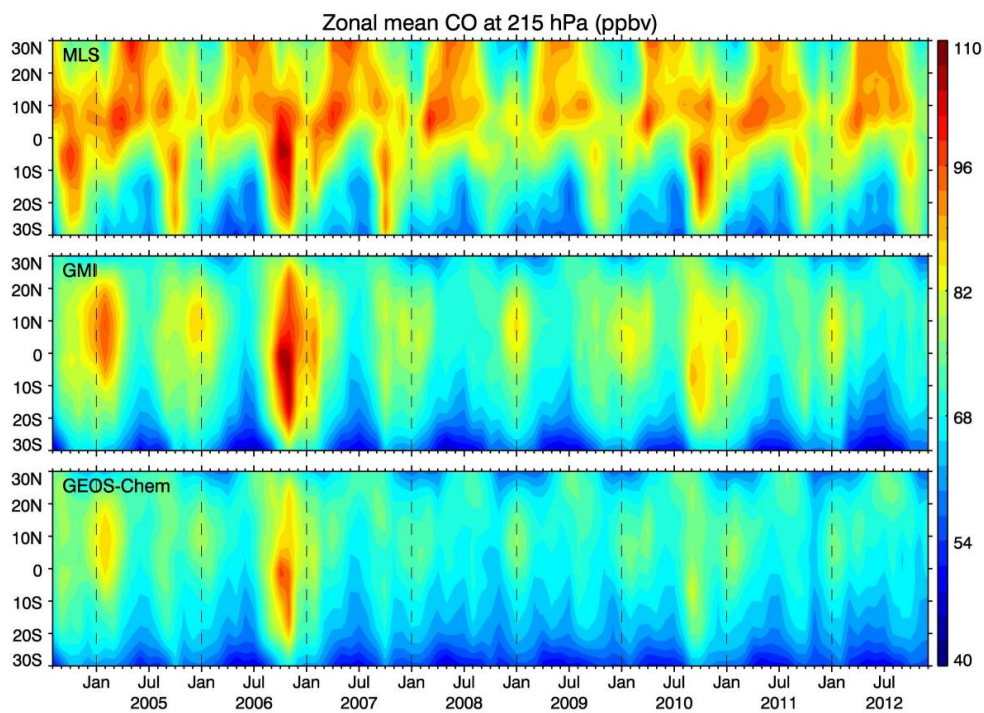


967



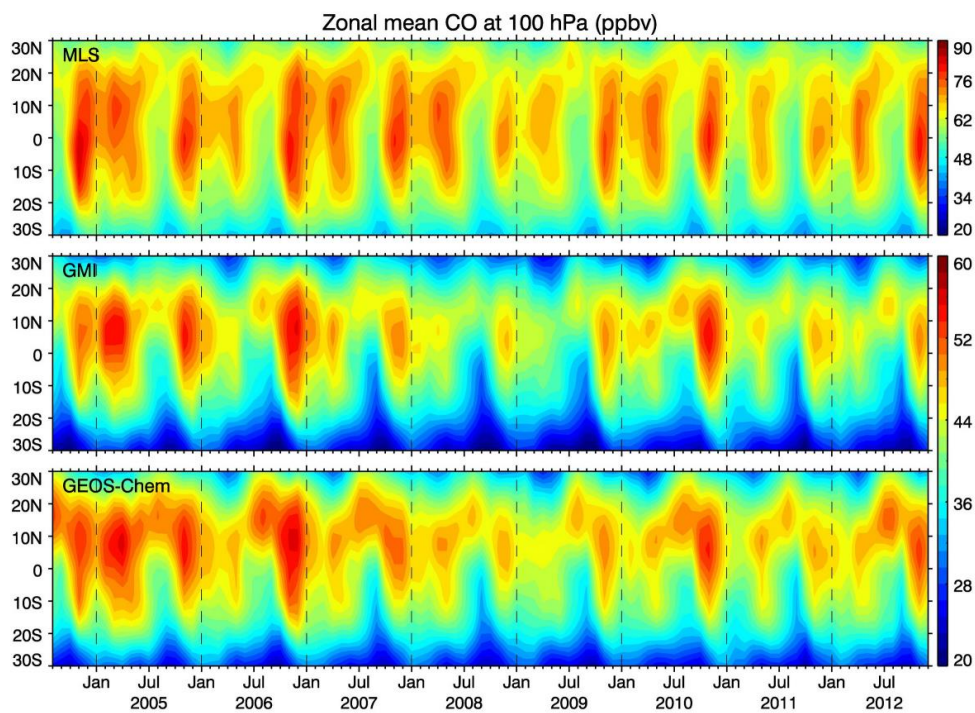
968

969 **Fig. 4.** Vertical/latitudinal distribution of zonal mean CO mixing ratio during different
970 seasons (DJF, MAM, JJA, and SON) from: (top row) MLS V4 data; (middle row) GMI
971 model simulation with MLS AKs applied; (bottom row) GEOS-Chem model simulation
972 with MLS AKs applied.



973

974 **Fig. 5.** Monthly variation of zonal mean CO mixing ratio at 215 hPa for August 2004 –
975 December 2012 from: (top row) MLS V4 data; (middle row) GMI model simulation with
976 MLS AKs applied; (bottom row) GEOS-Chem model simulation with MLS AKs applied.



977

978 **Fig. 6.** As in Fig. 5, but for CO mixing ratio at 100 hPa.

979

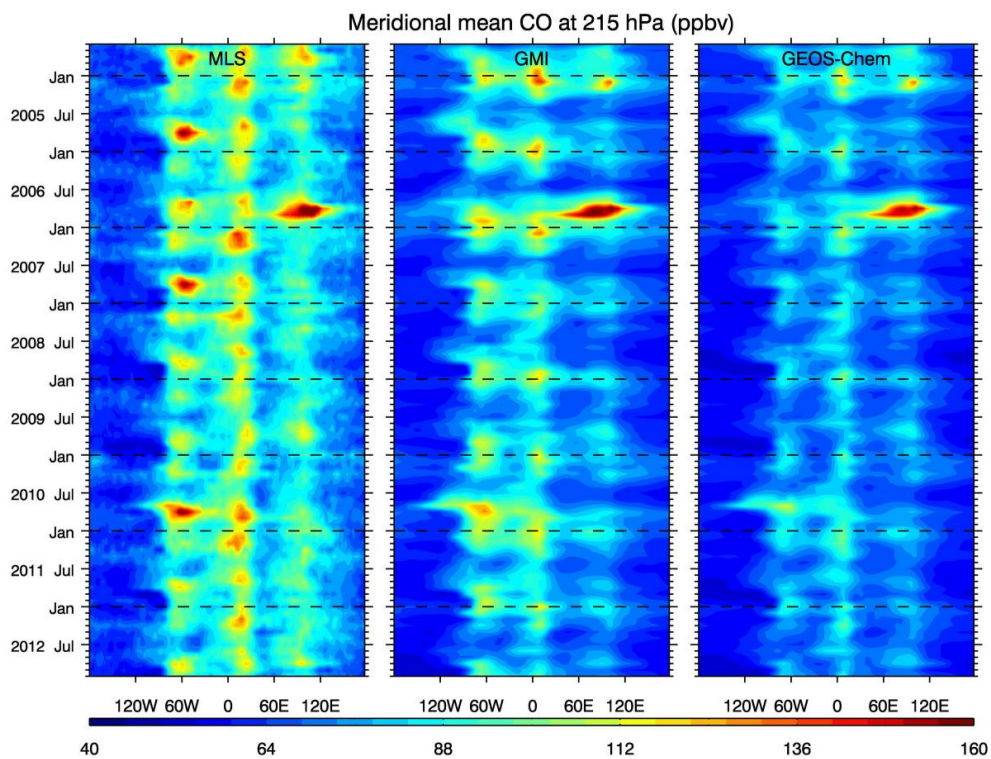
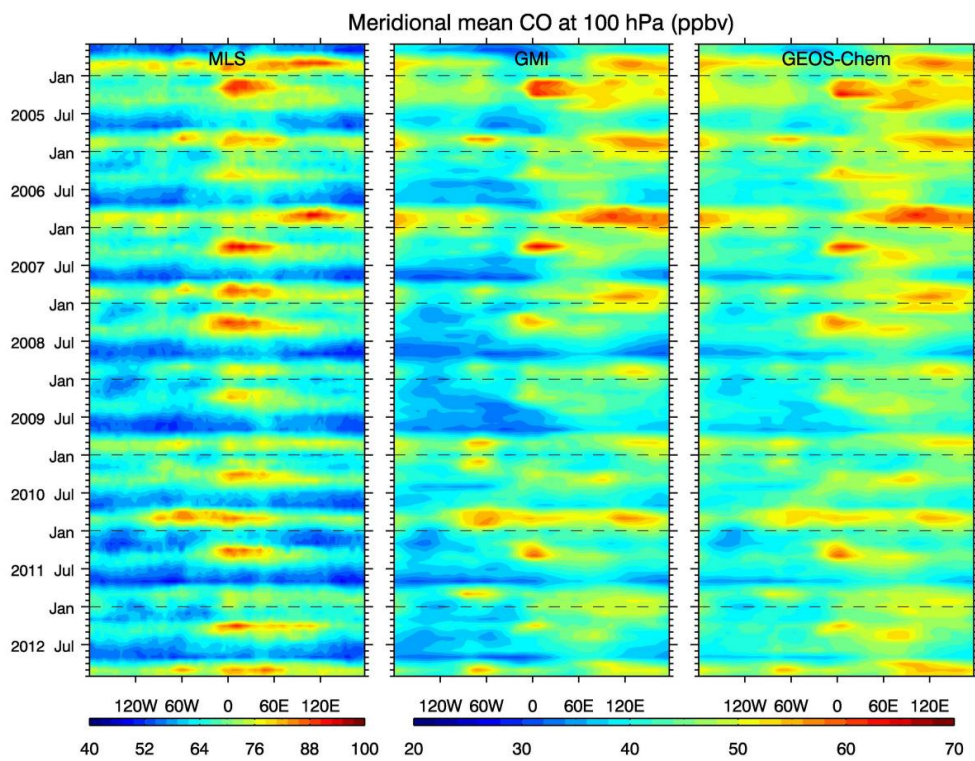
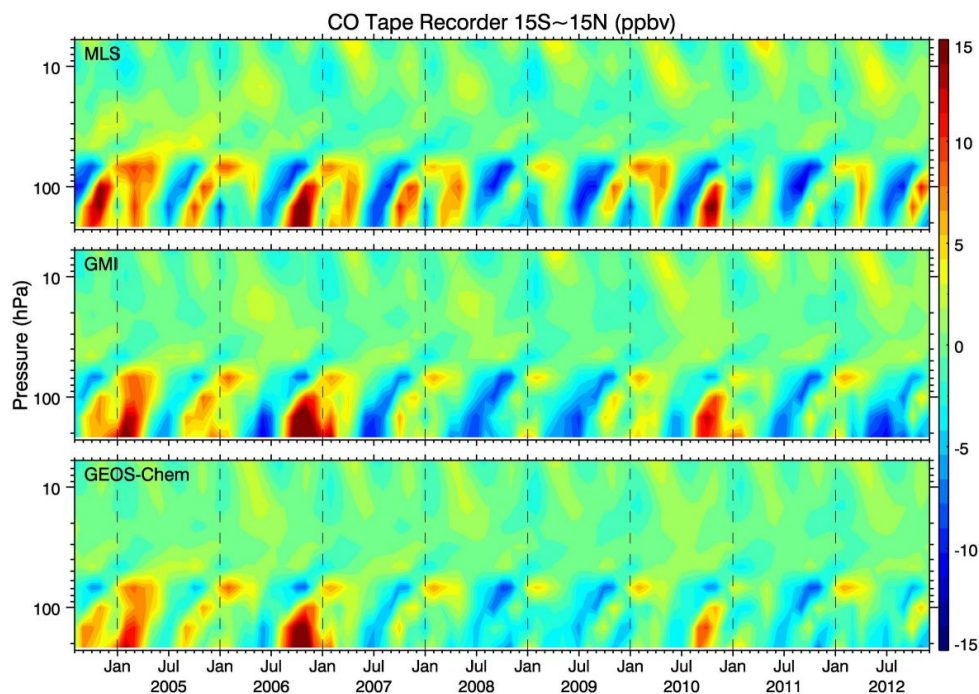


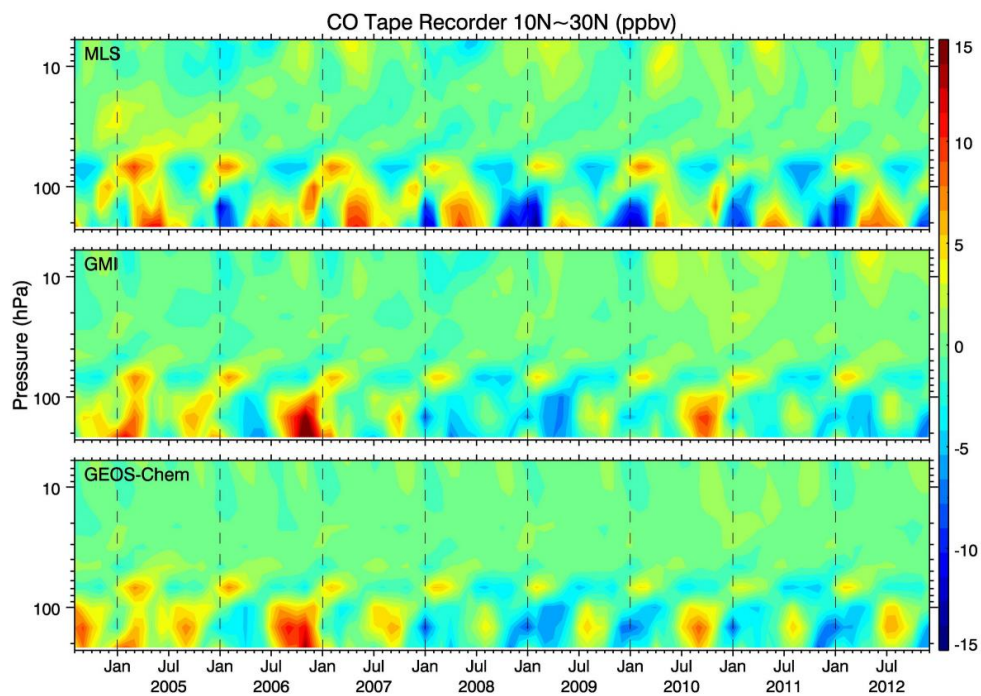
Fig. 7. Monthly variation of meridional mean (15°S – 15°N) CO mixing ratio at 215 hPa for August 2004 – December 2012 from: (left) MLS V4 data; (middle) GMI model simulation with MLS AKs applied; (right) GEOS-Chem model simulation with MLS AKs applied.





988

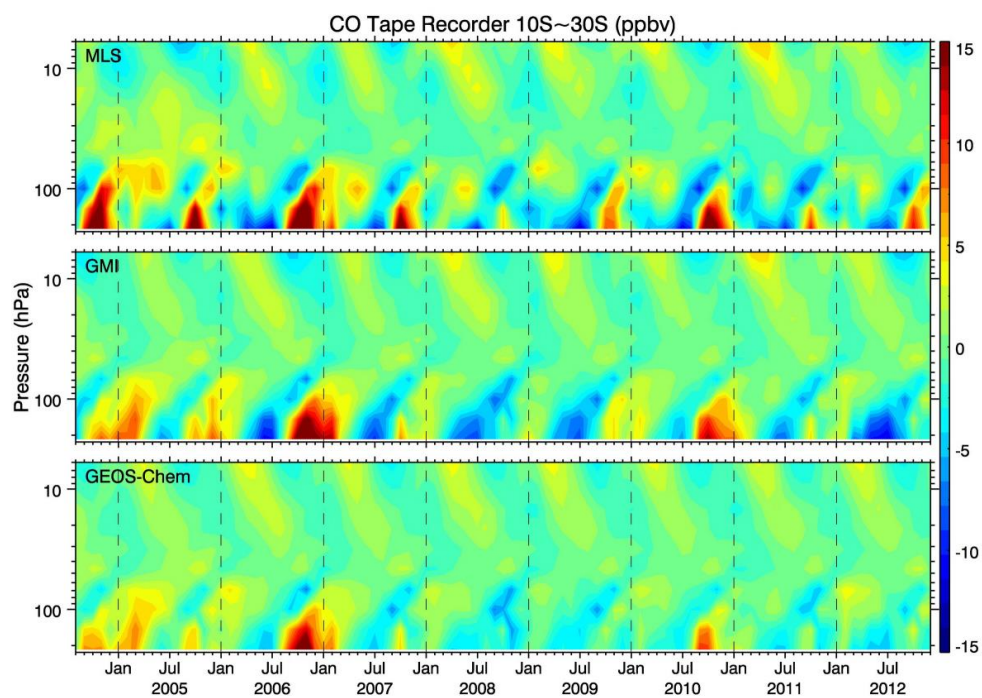
989 **Fig. 9.** Temporal variation of monthly mean CO deviations, zonally averaged over the
990 tropics (15°S–15°N), vertically from 200 hPa to 50 hPa for August 2004 – December
991 2012 from (top row) MLS V4 data; (middle row) GMI model simulation with MLS AKs
992 applied; (bottom row) GEOS-Chem model simulation with MLS AKs applied. An 8-year
993 mean (2005–2012) was subtracted from the monthly mean time series at each level for
994 MLS data and the two models' simulations.



995

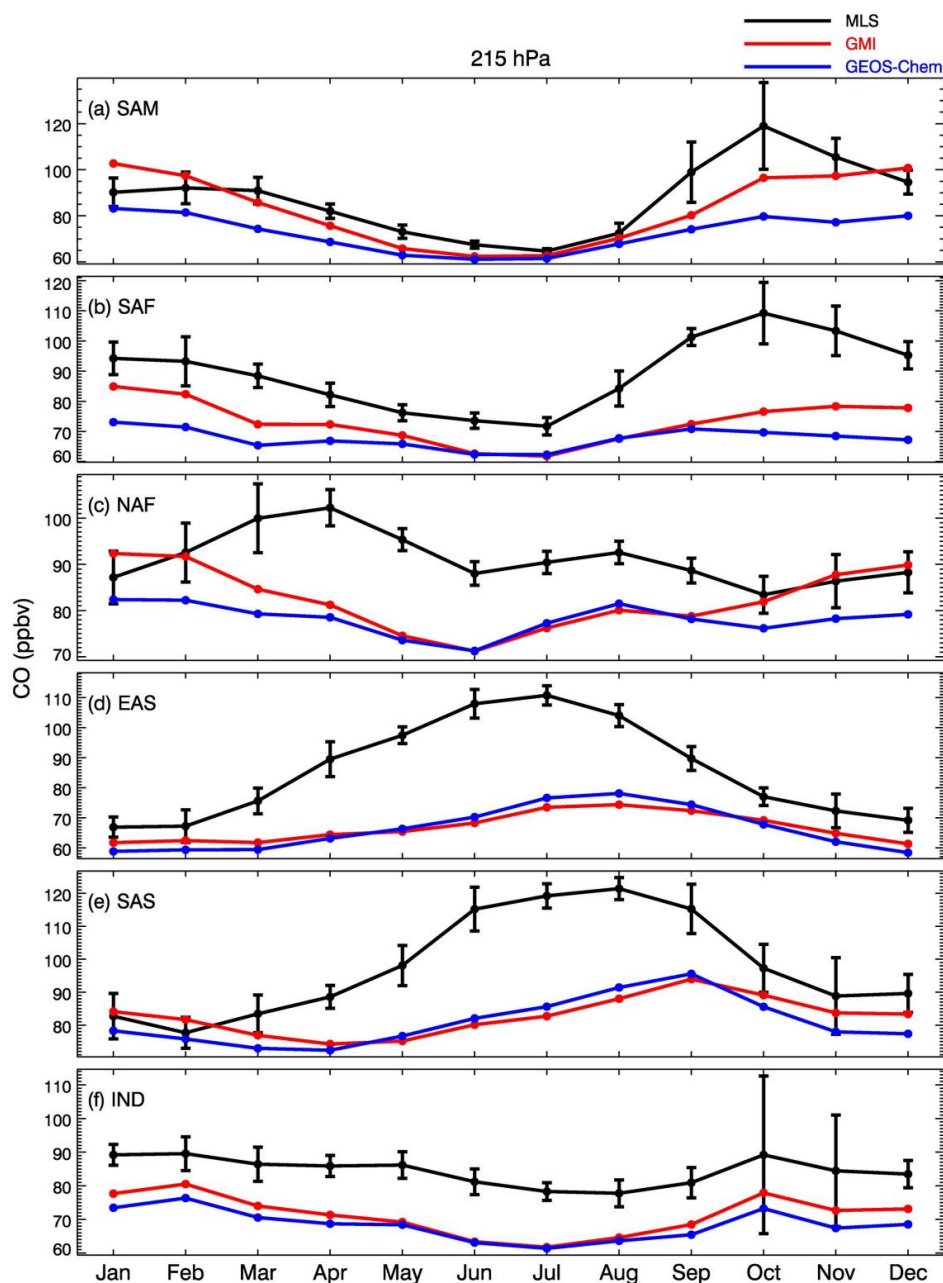
996 **Fig. 10.** As in Fig. 9, but over the northern subtropics (10°–30°N).

997



998

999 **Fig. 11.** As in Fig. 9, but over the southern subtropics (10°–30°S).

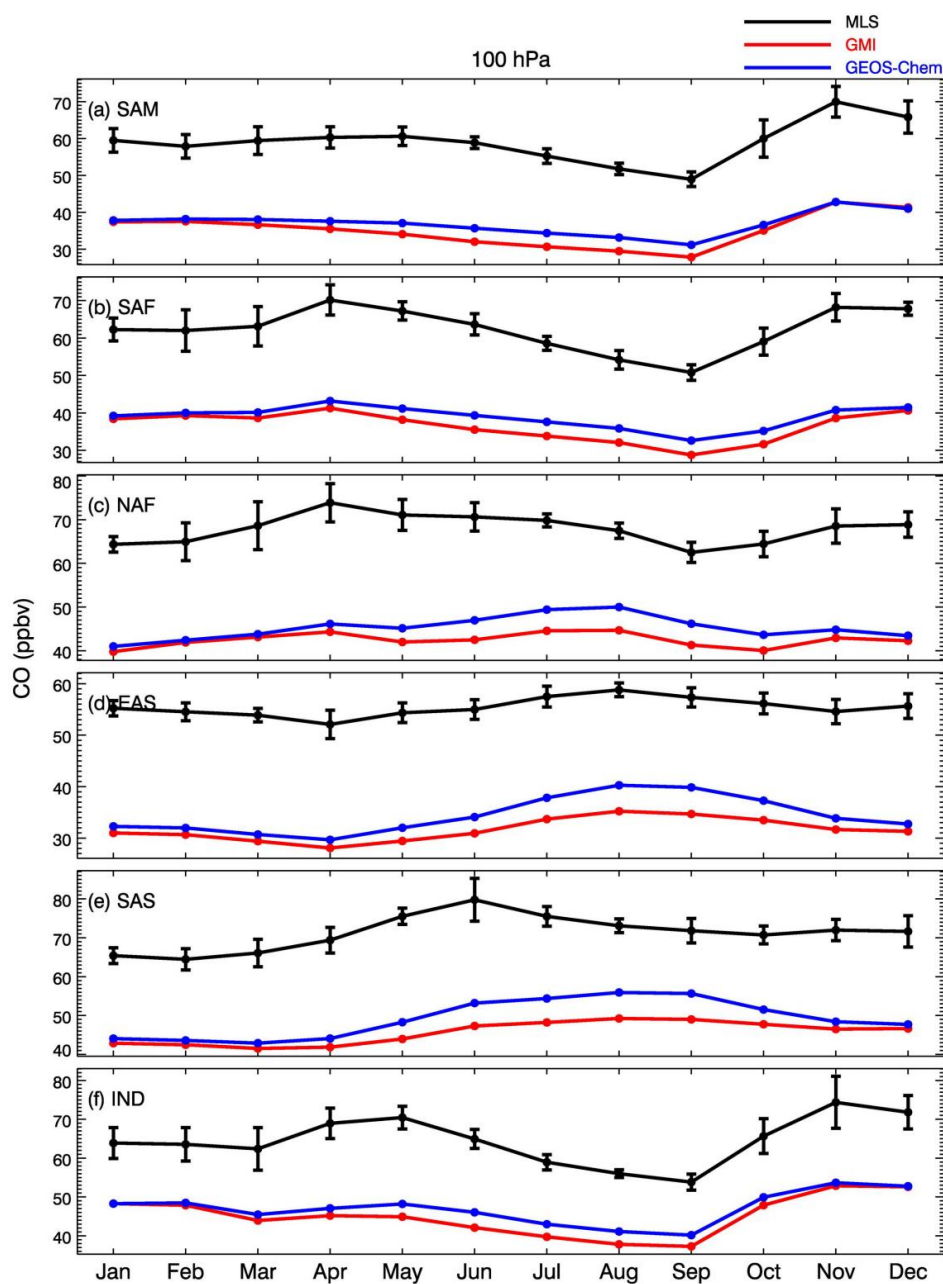


1000

1001 **Fig. 12.** Climatological (8-year) monthly mean of CO mixing ratio at 215 hPa from MLS
1002 V4 data (black line), GMI model simulation with MLS AKs applied (red line), and
1003 GEOS-Chem model simulation with MLS AKs applied (blue line) over the selected six



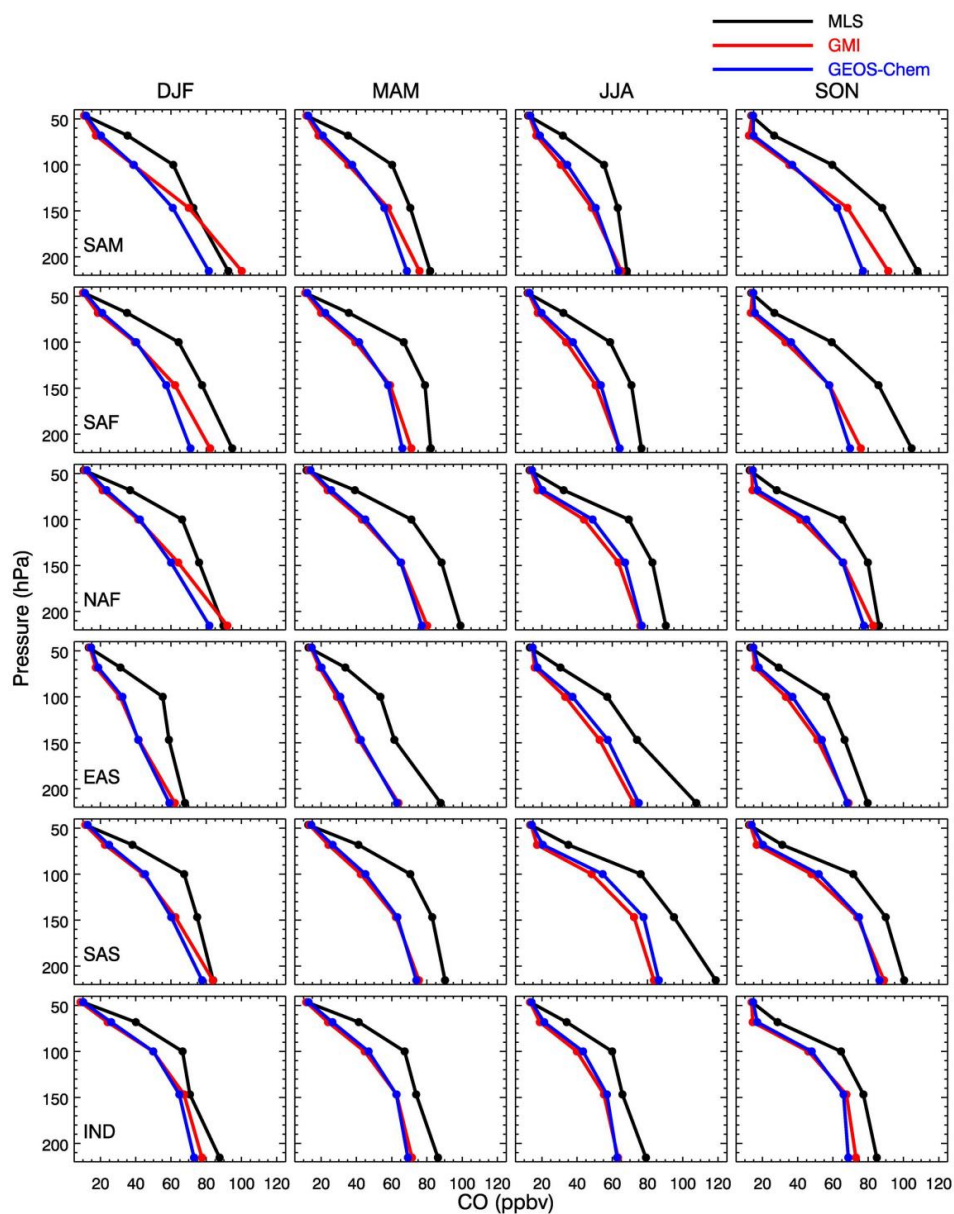
1004 regions: (a) South America, (b) Southern Africa, (c) Northern Africa, (d) East Asia, (e)
1005 South Asia, and (f) Indonesia. The error bars indicate ± 1 interannual standard deviation
1006 of the monthly mean CO from MLS V4 data.



1007



1008 **Fig. 13.** As in Fig. 12, but for CO mixing ratio at 100 hPa.

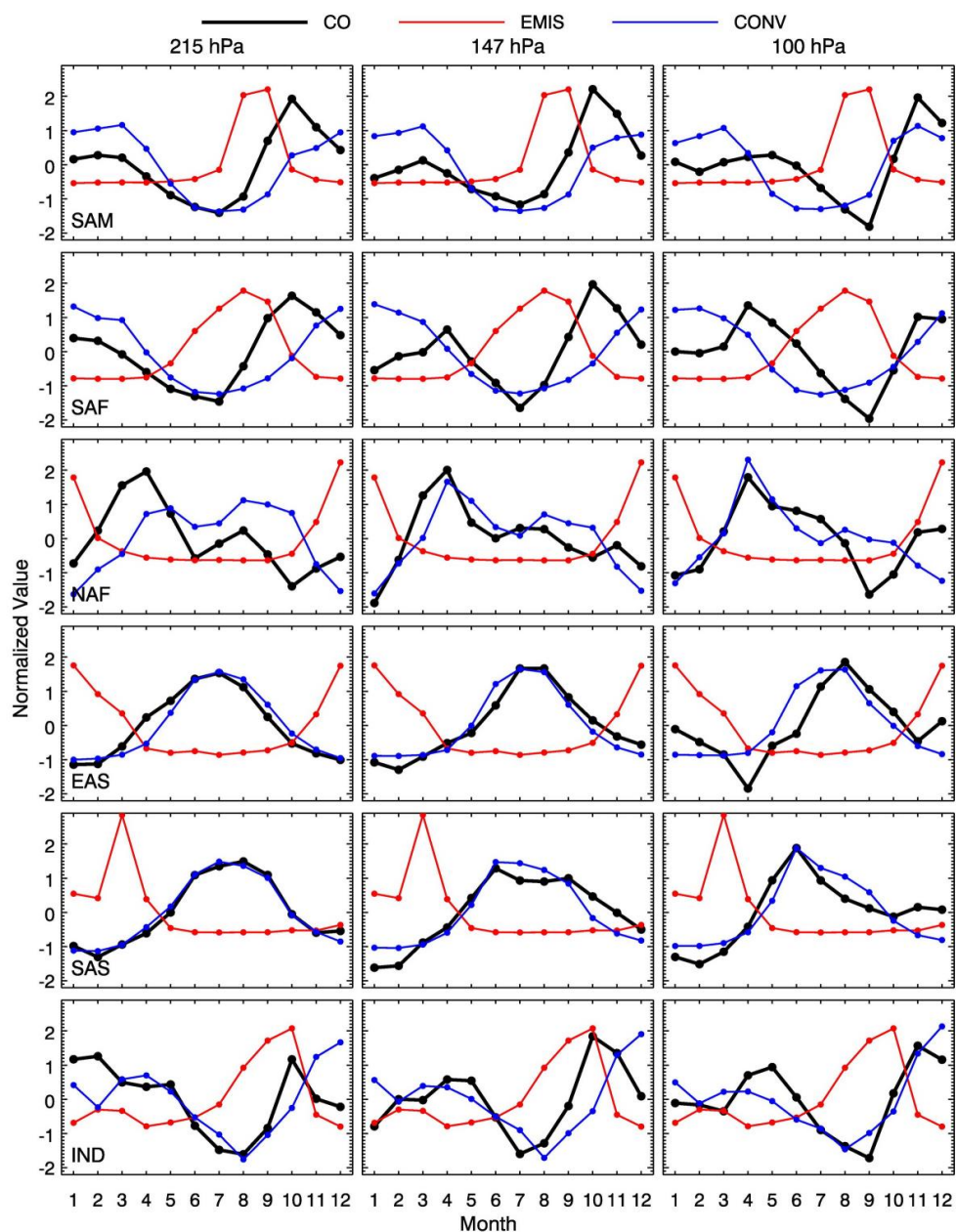


1009

1010 **Fig. 14.** Climatological (8-year) seasonal mean vertical profile of CO mixing ratio from
 1011 MLS V4 data (black line), GMI model simulation with MLS AKs applied (red line), and
 1012 GEOS-Chem model simulation with MLS AKs applied (blue line) over the selected six



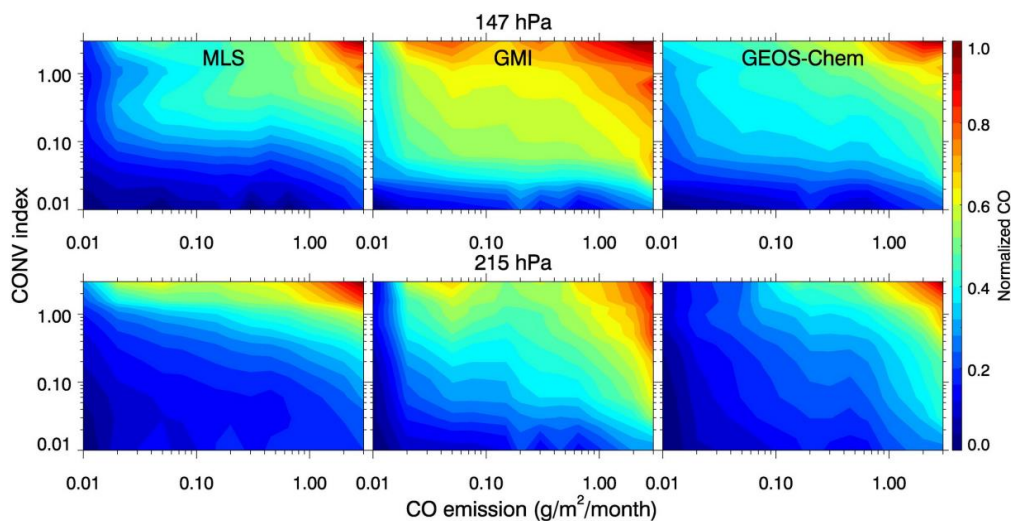
1013 regions: (top row) South America, (second row from top) Southern Africa, (third row
1014 from top) Northern Africa, (fourth row from top) East Asia, (fifth row from top) South
1015 Asia, and (bottom row) Indonesia.



1016

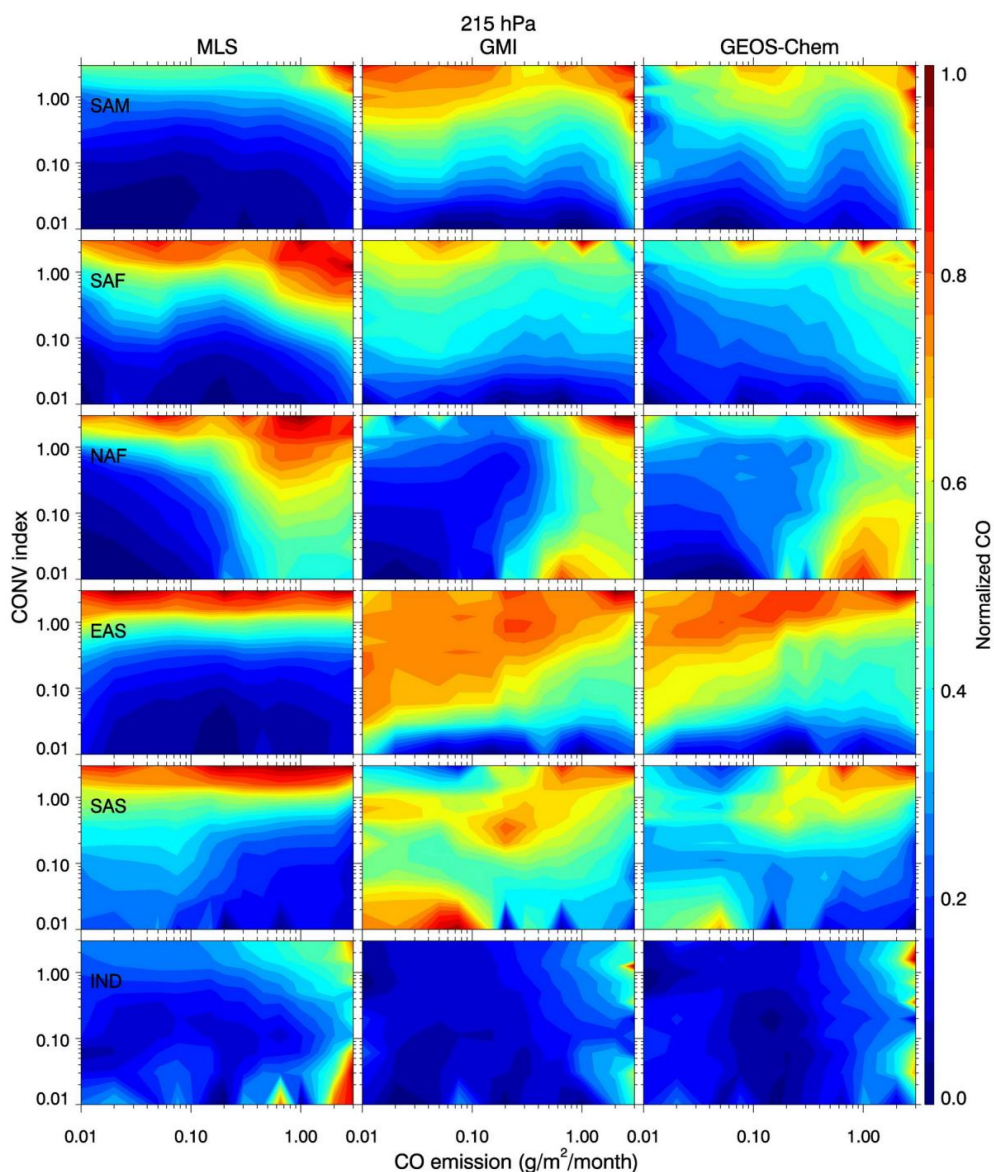


1017 **Fig. 15.** Climatological monthly mean of surface CO emission from GMI model (red
1018 line), ice water content (blue line) and CO mixing ratio (black line) at 215 hPa (left
1019 column), 147 hPa (middle column), and 100 hPa (left column) from MLS observation
1020 over six regions: (top row) South America, (second row from top) Southern Africa, (third
1021 row from top) Northern Africa, (fourth row from top) East Asia, (fifth row from top)
1022 South Asia, and (bottom row) Indonesia. Each variable is normalized for comparison.



1023

1024 **Fig. 16.** Contour plots of normalized CO mixing ratio at 215 hPa (top row) and 147 hPa
1025 (bottom row) over the tropics (30°S–30°N) from MLS observation (left column), GMI
1026 model simulation (middle column), and GEOS-Chem model simulation (left column)
1027 binned according to the surface CO emission (x-axis) and convective index (y-axis) at the
1028 same pressure level. See text for more details.



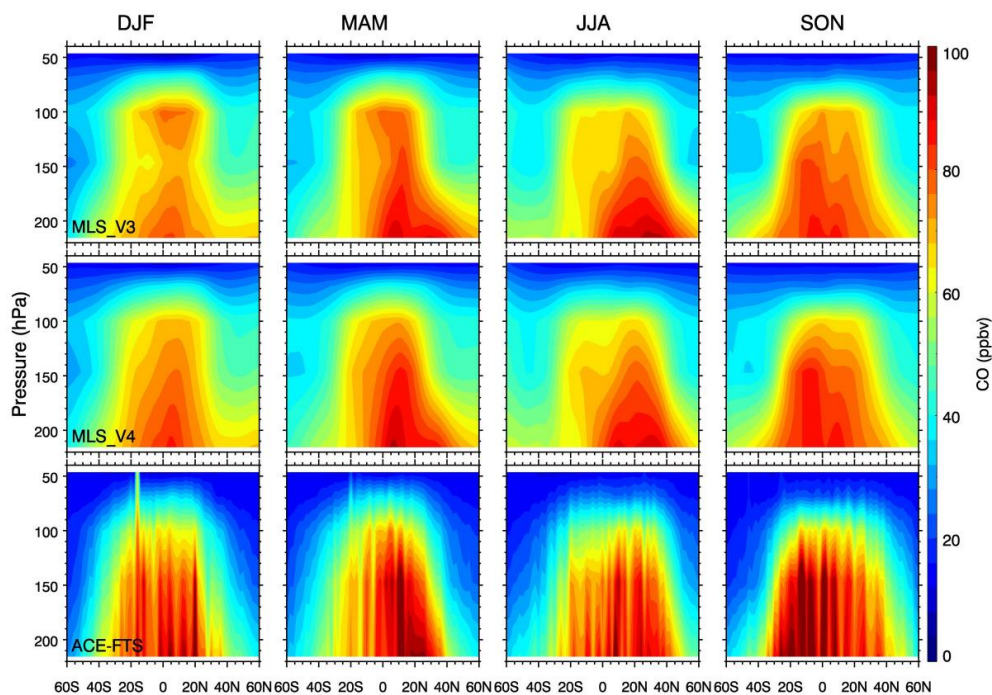
1029

1030 **Fig. 17.** Contour plots of normalized CO mixing ratio at 215 hPa over six regions: (top
1031 row) South America, (second row from top) Southern Africa, (third row from top)
1032 Northern Africa, (fourth row from top) East Asia, (fifth row from top) South Asia, and
1033 (bottom row) Indonesia, from MLS observation (left column), GMI model simulation
1034 (middle column), and GEOS-Chem model simulation (left column) binned according to



1035 the surface CO emission (x-axis) and convective index (y-axis) at the same pressure level.

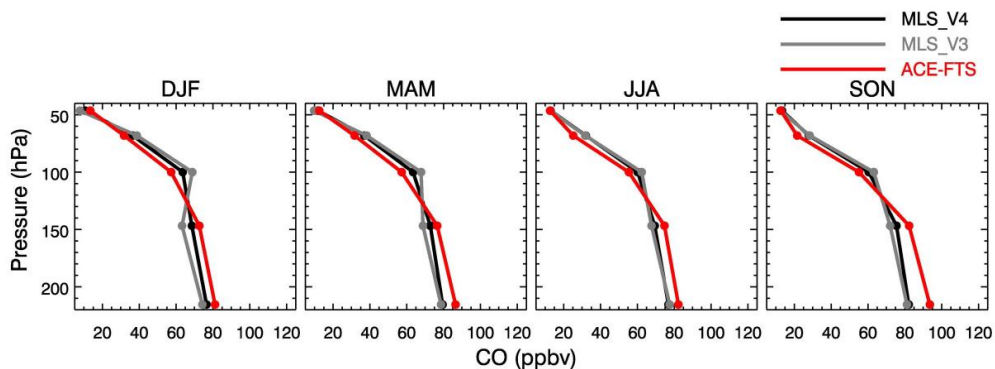
1036 See text for more details.



1037

1038 **Fig. A1.** Vertical distribution of zonal mean CO mixing ratio in the pressure-latitude
1039 cross-section during different seasons (DJF, MAM, JJA, and SON) from: (top row) MLS
1040 Version 3 CO data; (middle row) MLS Version 4 CO data; (bottom row) ACE-FTS CO
1041 data with MLS averaging kernels (AKs) applied.

1042



1043

1044 **Fig. A2.** Climatological (8-year) seasonal mean vertical profile of CO mixing ratio from
1045 MLS Version 4 CO data (black line), MLS Version 3 CO data (gray line), and ACE-FTS
1046 CO data with MLS AKs applied (red line) over the tropics (30°S–30°N).